Germanium-rich Silicon-Germanium Materials for Field-Effect Modulator Applications

by

Samerkhae Jongthammanurak

B.S. Materials Science and Engineering
Northwestern University, 2001

Submitted to the Department of Material Science and Engineering in Partial Fulfillment of the Requirements for the degree of

Doctor of Philosophy in Electronic, Photonic, and Magnetic Materials
at the
Massachusetts Institute of Technology

February 2008

© 2008 Massachusetts Institute of Technology. All rights reserved.

MASSACHUSETTS INSTITUTE OF TECHNOLOGY
JUN 16 2008
LIBRARIES

ARCHIVES

Signature of Author:_____
Department of Material Science and Engineering
January 11, 2008

Certified by:_____
Lionel C. Kimerling
Thomas Lord Professor of Material Science and Engineering
Thesis Supervisor

Accepted by:_____
Samuel M. Allen
POSCO Professor of Physical Metallurgy
Chair, Departmental Committee on Graduate Students

Germanium-rich Silicon-Germanium Materials for Field-Effect Modulator Applications

by

Samerkhae Jongthammanurak

Submitted to the Department of Materials Science and Engineering
on January 11, 2008 in Partial Fulfillment of the Requirements for
the Degree of Doctor of Philosophy in Electronic, Photonic and
Magnetic Materials

Abstract

The development of electric-field-induced optical modulation in the materials capable of monolithically integrated on silicon (Si) substrates offer the possibility of high-speed modulation in a pico second timeframe as well as low power consumption, key requirements for integrated modulator applications. This thesis presents a study of the Franz-Keldysh effect in germanium (Ge) layers epitaxially grown on Si substrates, by using free-space spectral responsivity measurement. Generalized Franz-Keldysh formalism and separately measured Ge material constants were used to calculate theoretical results, which were in agreement with experimental data. The Franz-Keldysh model predicts that the Ge layers on Si substrates will be the best material for phase modulation at nearly 2 μm wavelength, with a value of L_π of 3.8 mm and insertion loss of 0.4 dB.

In addition, this thesis presents the design of silicon-germanium (Si_xGe_{1-x}) electroabsorption and phase modulators at 1.55 μm wavelength from the Franz-Keldysh model. The composition optimized for electroabsorption and phase modulator applications is Si_xGe_{1-x} with a value of x~0.075 and 0.135, respectively. To achieve high-quality Ge-rich SiGe materials for the modulator applications, deposition of Si_xGe_{1-x} ($0.008<x<0.125$) buffers at low temperature was performed, and the growth kinetic was studied. The films were deposited on SiGe buffers to reduce lattice mismatch between the buffers and the remainders of the films, and were in-situ annealed in the same condition as was used for similarly grown Ge films for a reduction of threading dislocation density. $Si_{0.15}Ge_{0.85}$ *p-i-n* diodes and $Si_{0.15}Ge_{0.85}$ rib waveguides were fabricated. High leakage current in the $Si_{0.15}Ge_{0.85}$ *p-i-n* diodes was due to dislocation defects consistent with measured threading dislocation density from PV-TEM images, which showed threading dislocation density of approximately $1.5\pm0.5 \times 10^9$ cm^{-2}. The analysis shows that threading dislocation density below 5×10^7 cm^{-2} is required for high performance of *p-i-n* diodes. Furthermore, high optical loss was measured in $Si_{0.15}Ge_{0.85}$ rib waveguides and strip-load waveguides. The loss is due to light scattering at sidewalls and dislocations. Scattering from dislocations less than 1×10^8 cm^{-2} is required for loss below materials' interband absorption. This high threading dislocation density shows that the annealing condition used for Ge-on-Si is not effective in reduction of threading dislocation density in $Si_{0.15}Ge_{0.85}$. Si solutes/dislocations interactions in $Si_{0.15}Ge_{0.85}$ reduce glide velocity of dislocations as well as the possibility that dislocations run into and annihilate one another.

Thesis Supervisor: Lionel C. Kimerling
Title: Thomas Lord Professor of Material Science and Engineering

Acknowledgements

There are many people who I would like to thank for their support that make this work possible, help me learn many things about scientific research, and help me in many ways throughout the six and a half years at M.I.T.

First and foremost, I would like to thank my advisor, prof. Kimerling, for his guidance, understanding and encouragement. Discussion with him is always intellectually stimulating and encouraging. He values students' intellect. He has helped me to develop a deeper vision by asking me questions, listening to feedback and providing his insight. It always comes to my amaze how I learn more every time during the discussion. His support guides me to grow as a creative thinker and a scientist. Being his student is a privilege.

I would like to thank my thesis committee, Prof. Fitzgerald and Prof. Kärtner for sharing their insight and expertise with my thesis project. I feel privileged having an opportunity to learn from them.

I would like to thank Dr. Kazumi Wada for all his support. During his time at EMAT, I always learned more about Materials Science during the discussion with him and was amazed with his creativity and infinite idea. I would like to thank Dr. Jurgen Michel whose office door always welcomes the questions every day. I am thankful for his kind help. I would like to thank Dr. Xiaoman Duan for her support and kindness. She has been a great support to me, encouraged me not to give up in difficult time, gave me her compassion and shared with me her values, which I really appreciated. Having conversations with Dr. Anu Agarwal was always cheering me up. I am really grateful.

Dr. Anat Eshed has provided an insightful discussion on deposition and wonderful help with critical tool – the UHV/CVD reactors. Her conversation was always cheering up and supportive. I would like to thank Dr. Ching-yin Hong for her processing-related advice and support, especially when I just started my first set of experiments in MTL. Her office door was always welcoming when I dropped by after having encountered processing issues. I would like to thank Dr. Mark Beals for his tremendous help with the Sirius reactor and SEL. I really appreciated it.

I would like to thank Mr. Suguru Akiyama from Fujitsu for his design work of SiGe modulators and his insight on modulator subject. I learned a lot towards collaboration and discussion with him over a year. He shared his organizing skill which I should have practiced more and his insight in modulator and high-speed device. Thank you very much. I would like to thank Mr. Luciano Socci and Mr. Francesco Lopez from Pirelli who were of a great help in the beginning of the project. I would like to thank Dr. Douglas Cannon for his help in teaching me the first experiment of Ge and SiGe growth in MTL, which became the center of my thesis research.

I feel privileged to join EMAT as the same year as Jifeng Liu and Dave Danielson. Jifeng Liu has been an insightful research collaborator and a very good friend. I learned a lot about research through working with him. I would have not been surprised if one day he becomes a renowned professor. ☺ As also with Dave, I look up to his courage and initiation towards the renewable energy field. Sharing the office space with him for > four years is sometimes adventurous and definitely fun! Getting to know them is a privilege.

This thesis would not have been completed without tremendous technical support from MTL and CMSE staff. I am thankful to Vicky Diadiuk, Bernard Alamariu, Bob Bicchieri, Eric Lim and

Paul Tierney. They always provided helpful support to the project and shared with me their knowledge in microfabrication which cannot be found in textbooks.

For CMSE, I would like to thank Dr. Scott Speakman for his insights and expertise on X-Ray Diffraction, Dr. Yong Zhang for his help on TEM, Libby Shaw for AFM and Tim McClure for profilometer. They always provided suggestions that improved my experiments. I would also like to thank Mike Mori and Yu Bai from Fitzgerald group for their kind help, showing me their expertise on TEM sample preparation and double-tilt TEM techniques. I feel that I learned so much of on-hand experiments in material characterization from all of you.

The EMAT is a great place to learn, discuss research and make good friends. Thanks for making my laboratory experience enjoyable and memorable. Thanks to Lirong, Jing, Jessica, Sarah, Winnie, Xiaoxin, Mindy, Ellen, Lisa, J J, Jianfei, Jae Hyung, Kevin, Rong, Xiaochen, Dan, Donghwan, Mike, Sajan, Shoji, Victor, Wojtek, Yasuhiko, and Yasha.

There is a saying I recalled from somewhere, "Old friends are like gems that become more precious when time goes by. New friends are like presents that you give to yourself." First I would like to thank my old friends, E Rojana, Kaew Piyada, Pew Duangmanee and Yui Siraprapa, who have shared with me their kindness and courage since high school. My first year at MIT would have been much more difficult without tremendous help from the friends in the department, p Oy Pimpa, p Naan Panitarn, p Kob Nuwong, p Jess Jessada, p Ya Ariya and p Yot. They tutored me for the written and oral exams, gave me suggestions, cheered me up and brought all the fun times. I would also like to thank Albert Lok, Preston Li, Ratchatee and Wanida, who helped me with the preparation for the written exam. I would like to thank p Naan Panitarn, who was the warmest roommate I have ever had. She was always caring, taking care well of me when I was sick. She was indeed like my sister. I would like to thank Lek Wanida who has been a wonderful friend throughout the years at MIT with her ability in reading my mind sometimes, p Yong Waty who always shared with me her care and kindness and p Peng Warit who was always willing to help and taking care of everyone. Additionally, I would like to thank 'nong nong' and other friends who have enriched my life, filling my memories with joy and for their smiles that never faded away, Gift, Jane, Pond, Puye, Pu, Puk, Pin, Glao, Kob, Jelly, Mint, Taai, Tang, Aey, Bua, Fu, Joy, Prae, p Bo, p Jazz, Kit, Pun, Yeaw, Oh+, Jin, Ob, Kai, Pae, Aey, Aun, Aui, Bank, Bird, Hong, Pan, Pat, Petchie, Pee, Pok, Ricky, Ta, Ton, p Touch, Vee and Marcus.

I would like to thank my family (grandparents, parents, aunts, uncles and cousins) for their support. Above all, I am grateful of my parents who have been supportive and understanding through all my life. Their unconditional love and support led me way throughout the difficult time. My father always guided me by his wisdom but left plenty of room to let me be myself when my mother always cheered me up with her sense of humor. I am in debt to my parents who show me the greatness of their compassion and understanding. Without their support, I would not have come this far for Ph.D. This thesis is devoted to my parents.

Cambridge, Massachusetts, January 2008.

Table of Contents

List of Figures

List of Tables

Chapter 1: Introduction

1.1 Motivation

Fiber-optics technology has established a successful example for light-wave-based technology in long-haul data transmission. Photonics technology will be driven by electronic-photonic convergence and short reach interconnection of the distance less than 1 kilometer [1]. This shift in direction will ignite a change from data transmission (telecommunication) to information processing (computing) [1-2]. This shift will open high-volume applications that require a standard platform and infrastructures. An example of electronic-photonic integrated chips is shown in Figure 1.1 [1]. All devices are monolithically integrated on chips. Silicon-based devices are potential candidates for the monolithic integration, which can be fabricated by using complementary-metal-oxide-semiconductor processing technology (CMOS) infrastructure [1-6].

An example of applications of electronic-photonic integrated chips is optical transceivers integrated with electronics, giving a solution to limited bandwidth in emerging optical network access (ie. Fiber-to-the-Home) [1-6]. The electronic-photonic integrated circuits can also provide

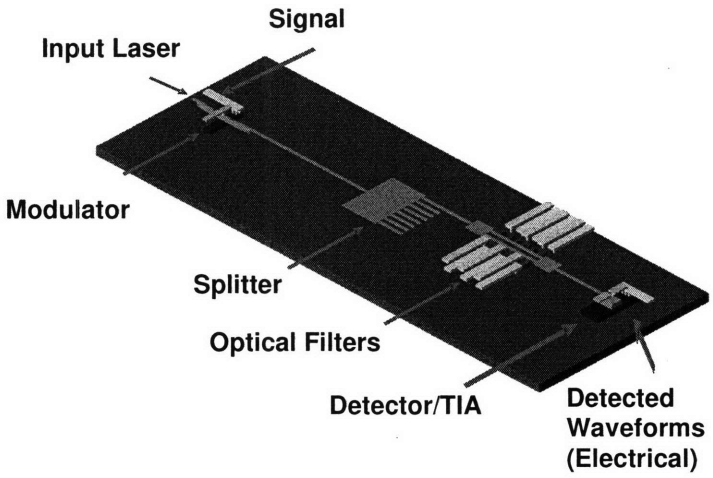

Figure 1.1 Schematic representation of an Electronic-Photonic integrated chips [1].

optical interconnects for CMOS electronics [1-6]. As the dimension of gate device scales down, the performance of integrated circuitry depends on the delay in electrical interconnections as shown in Figure 1.2. Since optical interconnections can carry larger bandwidth of data transmission compared to electrical interconnections, the optical interconnections can possibly solve this bottleneck problem and electronic-photonic integrated circuits can possibly be the solution.

In the integrated circuits, optical modulators are one of the key components for impressing information on light-wave. State-of-the-art silicon modulators use the plasma dispersion effect to modulate refractive index. The silicon modulators recently demonstrate up to 40 gigabits per second (Gb/s). Due to the carrier sweep-out or electron-hole recombination process, silicon modulators inherit limited modulation speed. The carrier-based devices require large driving voltage or power dissipation to manipulate carrier concentrations and achieve modulation speed over gigabit per second. Novelty functioning of optical modulators with low power consumption and large-bandwidth modulation demands a search for low-power modulators.

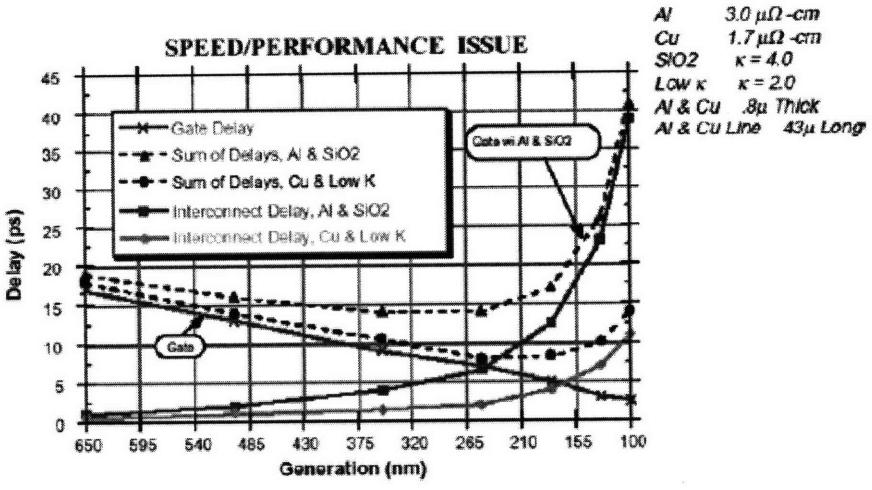

Figure 1.2 Performance delay versus dimension of gate devices [3].

1.2 Outline of Thesis

In an effort to find an alternative modulation effect for the modulator applications, this thesis focuses on studying the Franz-Keldysh effect in germanium (Ge), designing field-effect Ge-rich SiGe modulators and developing Ge-rich SiGe materials for field-effect modulator applications. Chapter two provides a survey on the performance of state-of-the-art silicon modulators. In section 2.1 key metrics for integrated modulators are discussed. Section 2.2 reviews free-carrier plasma dispersion effect in silicon. Section 2.3 reviews the performance of state-of-the-art carrier-based silicon modulators. The survey of silicon modulators shows that compact footprint and low power consumption are key traits for integrated modulators. These key requirements give motivation of developing field-effect modulators.

Chapter three describes the study of Franz-Keldysh-effect modulation in Ge films epitaxially grown on Si substrates (Ge-on-Si). We observed the change in absorption coefficients using spectral responsivity measured under the applied voltage on the Ge-on-Si *p-i-n* diodes. The Franz-Keldysh formalism was used to analyze the change in absorption. Ge-on-Si shows strong electroabsorption effect at 1647 nm wavelength. The derived electro-optic effect in Ge-on-Si is comparable to that in lithium niobate and indium phosphide. Calculation results show that Ge-on-Si will be the best material for Mach-Zehnder modulators at 1938 nm wavelength. The Franz-Keldysh model is used to design SiGe modulators for 1550 nm application.

Chapter four presents the design of Ge-rich SiGe electroabsorption and electro-optic modulators using the Franz-Keldysh model. To shift the operation wavelength to 1550 nm, silicon has to be added into germanium. The composition for electroabsorption and Mach-Zehnder modulator is 0.75% and 13.5% Si, respectively. Our calculation shows that a 50 μm long SiGe electroabsorption modulator yields an extinction ratio of 10 dB and a 3 dB bandwidth

of > 50 GHz. For Mach-Zehnder modulator, the waveguide dimensions and doping profiles were optimized to reduce the insertion loss. We predict that Mach-Zehnder modulator with two phase shifters of 15 mm long yield an extinction ratio of 3.7 dB with additional insertion loss of 1.5 dB.

Chapter five is devoted to Ge-rich SiGe deposition in ultrahigh vacuum chemical-vapor deposition (UHV-CVD) system for the modulator applications. To achieve high-quality Ge-rich SiGe materials for the modulator applications, deposition of Si_xGe_{1-x} ($0.008<x<0.125$) buffers at low temperature was performed, and the growth kinetic was studied. The films were deposited on SiGe buffers to reduce lattice mismatch between the buffers and the remainders of the films, and were in-situ annealed in the same condition as was used for similarly grown Ge films for a reduction of threading dislocation density. Results of strain and composition measured from the Si_xGe_{1-x} films are reported.

Chapter six is devoted to the device processing and characterization of $Si_{0.15}Ge_{0.85}$ *p-i-n* diodes and $Si_{0.15}Ge_{0.85}$ waveguides. Our study show that high threading dislocation density attributes to high leakage current and transmission loss. PV-TEM images show threading dislocation density of $\sim 1.7 \times 10^9$ cm^{-2}, in agreement with value of threading dislocation density estimated from bulk leakage current and transmission loss. We propose that Si solutes/dislocations interactions in $Si_{0.15}Ge_{0.85}$ reduce glide velocity of dislocations as well as the possibility that dislocations run into and annihilate one another and increases alloy yield stress. Reducing threading dislocations becomes more difficult in Ge-rich SiGe alloy compared to Ge.

Chapter seven is a summary of thesis and provides some tentative methods to reduce threading dislocation density in Ge-rich SiGe materials.

Chapter 2: Integrated Silicon Modulator Review

In this chapter we examined criteria for integrated modulators based on the metrics of integrated circuits. This chapter begins with a review of optical modulation physics in silicon and performance evaluation of state-of-the-art silicon modulators. Due to weak modulation effect, the silicon modulators require long Mach-Zehnder structures or large driving voltage. Our survey shows that none of silicon modulators fulfill all requirements of bandwidth, footprint and power dissipation, simultaneously. This conclusion suggests necessity for finding an alternative to the plasma dispersion effect, providing strong field-effect modulation in the materials capable of monolithically integrated on silicon substrates.

2.1 Key Traits of Modulators

Modulators are devices that facilitate an electrical-to-optical signal conversion. The modulators impress the information into light-wave by applying the voltage, which temporally changes the optical property of material. To evaluate modulator efficiency, we discuss common traits for integrated modulators as following [7]:

2.1.1 Footprint

Optical modulators for on-chip applications will be integrated at densities compatible with microelectronic integration. Area footprint for integrated modulators should not exceed 500 μm^2.

2.1.2 Driving Voltage and Power Dissipation

Driving voltage represents the voltage that modulators require for modulator operation. The driving voltage is quoted for a static (DC) or dynamic (AC) operation. In a DC operation of Mach-Zehnder modulators, driving voltage is quoted as V_π, which is the voltage required for a π-phase shift. The value of V_π depends on strength of modulation effect and waveguide dimension. Since the value of phase difference depends also on the modulator length L, the product $V_\pi L$ is

used to compare modulator efficiency. For on-chip application, driving voltage should be limited to 2V due to heat dissipation.

2.1.3 Bandwidth

Bandwidth represents the data capacity at which modulators can carry in a unit time. The bandwidth relates to the switching time between the "off" and "on" states, or vice versa. By convention, the bandwidth is taken as the difference between the upper and lower frequencies at which the modulation depth falls to 50% of its maximum value [8]. Bandwidth for integrated modulators should exceed bandwidth capacity of electrical interconnect at present (or larger than 10 GHz).

2.1.4 Extinction ratio

Extinction ratio (ER) represents the difference of light intensity between the "off" and "on" states. The extinction ratio in unit of decibel (dB) is expressed as

$$ER(dB) = 10\log\left(\frac{P_{out,\max}}{P_{out,\min}}\right) \tag{2.1}$$

where $P_{out,\max}$ represents optical power at highest transmission or "off" state and $P_{out,\min}$ represents optical power at lowest transmission or "on" state.

2.1.5 Insertion loss

Insertion loss represents the optical loss that modulators introduce into the system. This loss consists of the loss at the facet and the propagation loss in the waveguides. The system requirement limits maximum insertion loss of the devices less than 3 dB.

The traits of modulators and their specific criteria are summarized in Table 2.1.

Key criteria for integrated modulators are expressed in the figure-of-merit, bandwidth divided by

Table 2.1 Criteria for integrated modulators

Footprint	≤ 500 μm^2
Driving voltage	< 2 V
Power	≤ 1 mW/Gb/s
Bandwidth	> 10 GHz
Extinction ratio	> 3 dB (determined by Bit-Error-Rate)

a product of (power × device area) as in a following equation:

$$FOM = \frac{bandwidth}{power \times area} \tag{2.2}.$$

In addition to these previously mentioned criteria, a window of signal wavelength and modulator robustness to temperature fluctuation or fabrication error should be considered. In section 2.3, we will use these requirements to compare and evaluate the performance of state-of-the-art silicon modulators.

2.2 Free-Carrier Plasma Dispersion Effect in Silicon

Silicon is known as an indirect-gap material. The change in absorption coefficient due to the Franz-Keldysh effect in silicon is insufficient for modulator applications due to large optical absorption from its indirect gap [9]. Unlike lithium niobate, silicon has centrosymmetric structure and does not have the Pockels effect [9]. The most effective method for high-speed optical modulation in silicon is the free-carrier plasma dispersion effect. The change in real refractive index Δn and absorption coefficients $\Delta\alpha$ are induced by variations in carrier concentrations. At a wavelength of 1550nm, Δn and $\Delta\alpha$ are given by [10-12]

$$\Delta n = \Delta n_e + \Delta n_h = -\left[8.8\times10^{-22}\Delta N + 8.5\times10^{-18}(\Delta P)^{0.8}\right] \tag{2.3}$$

$$\Delta\alpha = \Delta\alpha_e + \Delta\alpha_h = 8.5\times10^{-18}\Delta N + 6.0\times10^{-18}\Delta P \tag{2.4}$$

where Δn_e is the refractive index change due to the change in electron concentration, Δn_h is the refractive index change due to the change in hole concentration, ΔN is the electron concentration change, and ΔP is the hole concentration change. The equation suggests an additional loss due to the variations of charged carrier concentrations. Change in hole concentration ΔP results in large change in real part of refractive index Δn compared to change in electron concentration ΔN. Value of Δn of 10^{-3} requires values of $\Delta P \sim 4\times10^{17}$ cm^{-3} or $\Delta N \sim 10^{18}$ cm^{-3}.

2.3 State-of-the-Art Silicon-based Modulator Review

Silicon modulators apply the free-carrier plasma dispersion effect to induce a change in real part of refractive index Δn. The modulators consist of rib waveguides that facilitate large optical mode in the silicon core. Large confinement of the optical mode in the core promotes the overlapping between the optical mode and electrical active region of Si, where Δn is induced. The large confinement enhances the change in effective index Δn_{eff} and reduces the driving voltage. Si rib waveguides are used to construct state-of-the-art Si modulators that demonstrate modulation speed in gigabit per second (Gb/s). Mach-Zehnder structure or ring resonator structure is used to convert phase retardation into optical intensity modulation. Figure 2.1 shows schematic diagrams of (a) Mach-Zehnder structure and (b) ring-resonator structure.

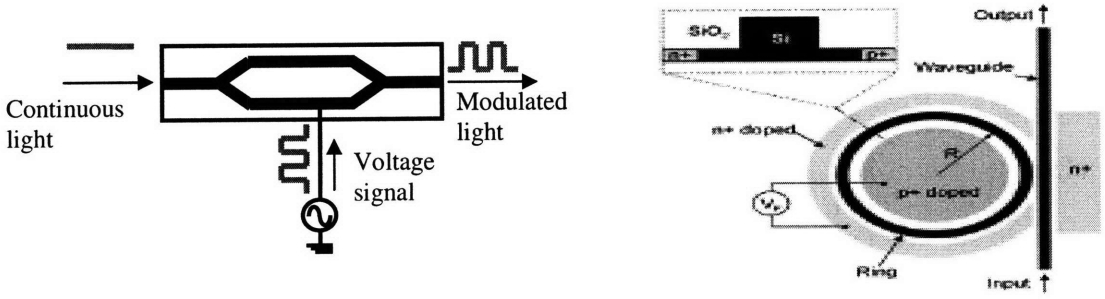

Figure 2.1 Schematic diagrams of (a) Mach-Zehnder structure and (b) ring-resonator structure [19].

We organize the summary for silicon modulators by Mach-Zehnder structure (MZ) and ring-resonator (RR) structure.

2.3.1 Mach-Zehnder structure (MZ)

The first version of silicon modulators operating at Gb/s is achieved by Intel [12]. Structure of metal-oxide-semiconductor (MOS) is used in controlling carrier distribution. The MOS structure consists of an embedded thin oxide layer inside a core of silicon waveguide. External voltage applied to the oxide layer creates variations in carrier concentrations, which modulate index of refraction. In the later version of this MOS device, part of waveguide made of polysilicon is replaced with crystalline silicon and the dimension of waveguide is reduced to improve the overlapping between the guided mode and free carriers [13]. This version of the 3500 μm long MOS-based device shows ~3.8 dB modulation depth at 10 Gb/s. At this bandwidth, a DC voltage of -3.3 V and an AC voltage swing of 1.4 V is applied. The estimated power is ~ 700 mW.

Modulation operation with *p-i-n* junctions under reverse-bias has been demonstrated. Luxtera reports silicon modulator operating under reverse bias [14]. The 4400 μm long device demonstrates modulation at 10 Gb/s. This modulator is driven by push-pull operation with 2.5 V on each phase shifter with the estimated power of ~ 575 mW. Intel demonstrates silicon Mach-Zehnder modulator operating under reverse bias [15-16]. They use the electric-field in depletion region under reverse bias to control charged carriers. The 1000 μm-long *pin*-based device demonstrates a 30 Gbit/s bandwidth with ~0.44 dB extinction ratio. At this bandwidth, a DC voltage of 3.5 V and a 6.5 V peak-to-peak is applied. The estimated power is ~800 mW. This *p-i-n* junction-based modulator demonstrates a benchmark for the largest bandwidth capacity. The latest experimental progress in Mach-Zehnder modulators is reported by IBM. Their 200 μm long Si modulators achieve a data bit rate of 10 Gbit/s under a 1.2 V peak-to-peak pattern with pre-emphasis pulses of 3.5 V peak amplitude [17]. The Si rib waveguides in these modulators

have ultra-compact cross sectional area of approximately 0.12 μm^2 as compared to 1 μm^2 of other Si modulators. Due to the ultra compact cross sectional area of Si rib waveguides, the free carriers flow through the entire height of the rib waveguides and the free carrier/optical mode overlap is ensured. The compact structures results in low power dissipation compared to that in the previously demonstrated Si MZ modulators. At modulation of 10 Gbit/s, DC and RF power is 287 μW and 51 mW, respectively. The modulators from IBM are currently the most compact MZ modulators with data bit rate of 10 Gbit/s.

The design of Si Mach-Zehnder structure that promises efficient performance is reported by MIT. Gan et al. propose Si-based Mach-Zehnder modulators with split ridge waveguides for good thermal heat sinking and *p-i-n* junctions for carrier injection [18]. The device is under forward bias operation. The bandwidth is improved by reducing the carrier lifetime by means of ion bombardment and doping in the intrinsic region of the *p-i-n* structure. This device is designed for 24 GHz or for the bandwidth larger than 10 Gb/s bandwidth. The driving voltage is a DC voltage of 2 V and an AC voltage of 1 V. Estimated powers are 500 mW (DC) and 76 mw (AC).

2.3.2 Ring-Resonator structure (RR)

Silicon ring resonators represent a benchmark in Si modulators for the smallest footprint and power consumption. The ring resonator structure (RR) is designed for strong optical confinement and enhanced sensitivity to the change in refractive index Δn without increasing the device length [19]. *p-i-n* junctions are embedded across the 12 μm long diameter ring resonator to create variations in carrier concentrations. The Si ring resonator operates under forward bias which injects carriers into the waveguide core. The ring resonator modulator demonstrates a 9dB extinction ratio at a bandwidth of 12.5 Gbit/s. To increase the bandwidth, a pre-emphasis pulse of voltage is used to extract the carriers [20]. This pulse reduces the delay in optical rise time, giving an increase in bandwidth. Estimated power consumption for the ring resonator modulator

is approximately 18.7 mW. The particularly low power consumption is due to small footprint of the device.

In summary, Intel's Mach-Zehnder-based modulator sets the benchmark of 30 Gbit/s bandwidth. Due to its large footprint, power consumption is in several hundred milliwatt range. The Si ring-resonator-based modulator has the smallest footprint and consumes the least power dissipation. Due to the ring resonator characteristics, the operation bandwidth is relatively narrow compared to Mach-Zehnder-based modulators. The operating wavelength of ring resonators is also sensitive to the temperature change and fabrication error.

2.3.3 Comparison

Table 2.2 summarizes the characteristics of the Si modulators. The power refers to the value of power for an AC operation, corresponding to the bandwidth or data bit rate reported in Table 2.2. We used the figure-of-merits in section 2.2 to evaluate the modulator performance. Quantity in grey labels shows the performance that does not meet the requirement from Table 2.1. The remainder shows the performance that meets the requirement.

Table 2.2 Performance summary of Si modulators reported in the literature

	Intel MZM (experiment)	Luxtera MZM (experiment)	IBM MZM (experiment)	MIT MZM (theory)	Cornell RR (experiment)
Device Length	1000 μm	4400 μm	200 μm	2500 μm	14 μm
Bandwidth	20 GHz	-	-	24 GHz	~ 8 GHz
Data bit rate	30 Gbit/s	10 Gbit/s	10 Gbit/s	-	12.5 Gbit/s
Voltage	6.5 V_{pp}	5V	1.2V_{pp}, 3.5$V_{pre\text{-}emphasis}$	1V_{AC}	8V_{pp}
$V_{\pi}L$ (V-cm)	~ 4	-	~0.036	~ 0.5	-
Extinction ratio	~ 1-2 dB (estimated)	-	-	> 10 dB	~ 9 dB
Power	800 mW	575 mW	0.287 mW_{DC} 51 mW_{RF}	2.5 W_{DC} 380 mW_{AC}	18.7 mW

We plot the traits of each modulator in term of (power consumption × device area) vs. bandwidth in Figure 2.2. Dash lines mark boundary of the area where the traits' values fulfill the criteria of integrated modulators. The performance data of lithium niobate ($LiNbO_3$) and InGaAs modulators are also plotted to compare with that of the silicon modulators. Figure 2.2 shows comparison of modulator performance. Among experimental data, Intel's modulators show the largest bandwidth, which meets the bandwidth requirement. However, due to the large footprint, the power dissipation in these Intel Mach-Zehnder modulators is relatively high at almost 1 W. Recent IBM's Mach-Zehnder modulators of 200 μm in length demonstrate a smaller power dissipation of 51 mW at 10 Gbit/s. Ring-resonator modulators are promising devices in term of compact footprint, low power dissipation and its potential for high-speed application. However, the ring-resonator modulator has a few drawbacks of relatively narrow bandwidth, temperature sensitivity and fabrication tolerance.

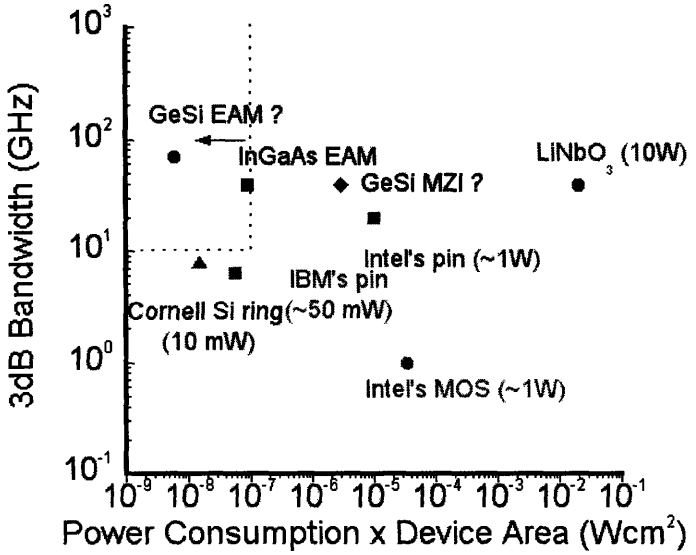

Figure 2.2 Summary chart of modulator performance.

2.4 Summary

Key metrics and criteria for integrated modulators have been discussed. State-of-the-art Si Mach-Zehnder modulators demonstrate large bandwidth whereas Si ring-resonator modulators in micrometer-scale demonstrate gigabit-per-second modulation speed. Nevertheless, their performance does not simultaneously fulfill all criteria for integrated modulators due to carrier-induced small change in real part of refractive index and diffusion-limited slow modulation effect in Si. Alternative field-induced modulation effect in Ge monolithically integrated on Si may provide a solution for on-chip low-power modulator applications.

Chapter 3: Franz-Keldysh Effect in Germanium layers grown on Silicon substrates

In this chapter, we describe our experimental study of the Franz-Keldysh effect in Ge-on-Si. The Franz-Keldysh effect is the field-induced effect that introduces large change in real part of refractive index Δn compared to the free-carrier plasma dispersion effect. The Franz-Keldysh effect is capable of modulation in pico-second timeframe due to non-carrier mechanism. The data were analyzed by using the generalized Franz-Keldysh formalism. The results from the calculation are in agreement with the experimental findings.

3.1 Review of Franz-Keldysh Effect

The Franz-Keldysh effect describes the field-dependent change of absorption coefficient in semiconductor. We can understand the Franz-Keldysh effect with the assistance of Figure 3.1 from Ref. [21]. The Franz-Keldysh effect is divided into two categories: 1). weak absorption regime or photon energy less than band gap E_g and 2). photon energy larger than band gap. Under the applied electric field F, the energy bands are tilted. This tilting assists the electron tunneling into the energy gap. The points marked A and B represent the turning points, where the tunneling takes place or electron wave function changes from oscillatory to decaying behavior. When the applied electric field F increases, the horizontal distance AB decreases. As a result, the overlapping of the two wave functions is enhanced. This overlapping represents probability of electron transition or photon absorption. Absorption coefficient α is expected to increase with value of F. For another case at which photon energy larger than that of bandgap E_g, the two wave functions are made of an incident wave and a reflected wave. The relative phase of the two waves varies with the applied field F. The interference of the incident and reflected waves results in an oscillatory behavior of the absorption coefficients.

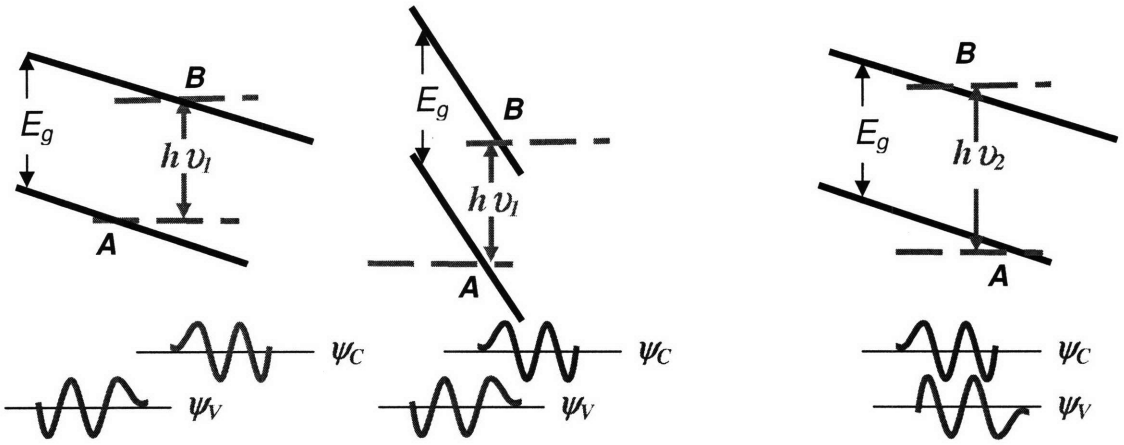

Figure 3.1 Schematic diagram showing energy-band for the Franz-Keldysh Effect. (a) The case for photon energy larger than the band gap and (b) photon energy smaller than the band gap [21].

3.2 Franz-Keldysh Effect in Tensile-Strained Ge-on-Si Films

The Franz-Keldysh effect in bulk germanium (Ge) was first reported by Frova et al [22]. They observed the increase in absorption under the applied electric field in the weakly absorbing regime where photon energy is less than the direct bandgap. Here, we report first observations of the strain-enhanced Franz-Keldysh effect in Ge layers directly grown on Si substrates (Ge-on-Si). We have previously studied the strain-induced optical characteristics of epitaxial Ge-on-Si films for detector applications [23-26]. Tensile strain in these Ge films introduces a reduction of the direct energy gap, and a decrease in the separation between the direct and indirect energy gaps which results in reduced α below the direct gap. We anticipated that in the weakly absorbing regime (energies lower than the direct band gap), a strain-enhanced increase in the joint density of states could yield a significantly enhanced electro-optic effect. We have analyzed diode spectral responsivity data using generalized Franz-Keldysh formalism and experimentally derived parameters based on strain-induced direct band-gap reduction under the biaxial stress [26].

3.2.1 Experimental procedure

The Ge *p-i-n* photodiodes used in this work were fabricated from 1.3μm thick undoped Ge layer on a p+ Si(100) substrate with boron concentration > 10^{19} cm^{-3}. The Ge epilayer was under 0.20% tensile strain [26]. Phosphorus was implanted into a polysilicon layer that was deposited on the top of the Ge epilayer to create a *p-i-n* structure. The phosphorus peak concentration was approximately 10^{20} cm^{-3}. Ge films on Si substrates were deposited by first depositing a 60 nm thick Ge layer at low temperature and remainder of the films at high temperature. Threading dislocation density in the films is reduced by cyclic thermal annealing. Inset of Figure 3.2 shows a schematic cross-section of *p-i-n* photodiodes fabricated of epilayer Ge on Si substrates. Details of Ge growth and diode fabrication have been reported in [27]. The electrical properties and doping profile of the diode were analyzed using current-voltage (I-V) and capacitance-voltage (C-V) characteristics. Figure 3.2 shows I-V characteristics of Ge-on-Si *p-i-n* photodiodes measured under dark current. Note that positive range of applied voltage on the right hand-side is reverse bias. The leakage current density at 2 V reverse bias is approximately 0.02 A/cm^2.

The doping level in the *i*-region calculated from C-V data was ~ 10^{16} cm^{-3}, or about three orders of magnitude lower than the n+ phosphorus and the p+ boron doping levels. Accordingly, electric field under applied reverse bias was uniform in the Ge epilayer. The electric field magnitude in the i-region was calculated by subtracting the potential drop due to series resistance from the externally applied voltage. The electronic properties of device were modeled using a one dimensional finite-difference simulator (PC1D). External biases of 0 and 5 V were applied to the diode, corresponding to electric fields of 14 and 70 kV/cm in the Ge *i*-layer, respectively. The absorption coefficient α was calculated from the photodiode responsivity (R) using [27]:

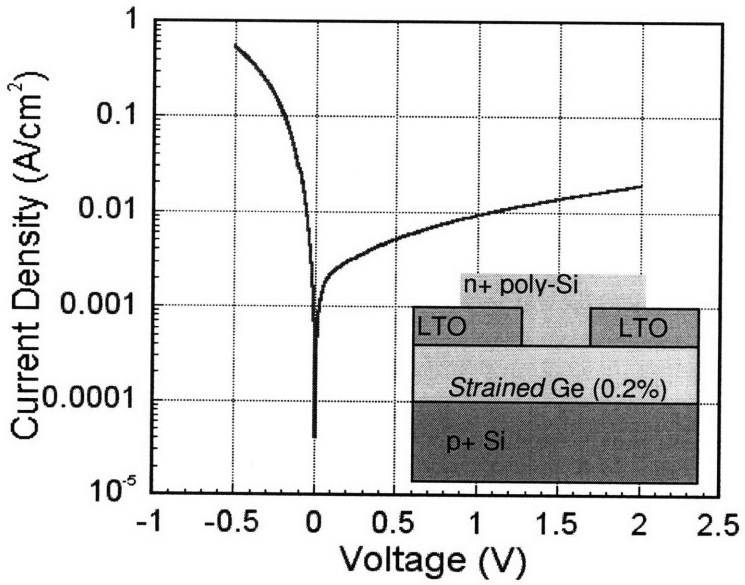

Figure 3.2 I-V characteristics of Ge-on-Si photodiodes under dark current. The inset shows schematic diagram of cross-section of the photodiodes.

$$\alpha = -\frac{1}{t_{Ge}} \ln\left(1 - \frac{1240}{\lambda(nm)} \bullet \frac{R}{(1-R_{refl})}\right), \tag{3.1}$$

where R_{refl} is the reflectance of the photodiodes, and t_{Ge} is Ge depletion width under reverse bias. The change in surface reflection upon the application of bias was negligible.

3.2.2 Spectral Responsivity Results

The results represent the first observation of the strain-enhanced electro-optic effect in strained Ge films on Si substrates. The spectral responsivity of the Ge *p-i-n* diode was measured under electric fields of 14 and 70 kV/cm. Figure 3.3 shows the spectral responsivity difference ΔR observed upon the applied electric fields compared with the model for ΔR using Equations (3.1) and (3.2). The responsivity spectrum shows characteristic oscillation associated with the

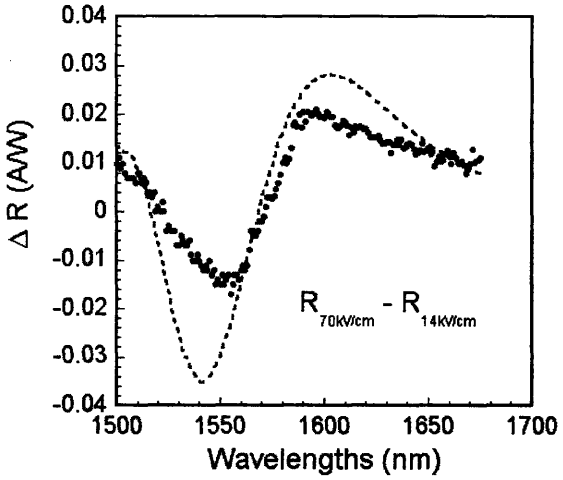

Figure 3.3 Observation of the Franz-Keldysh effect for the strained Ge films on Si substrates. Difference in responsivity spectra shows the characteristics of the Franz-Keldysh effect. Dots represent experimental data. Dash lines represent the data from the model.

Franz-Keldysh effect. At wavelengths longer than 1580 nm or that corresponding to the direct band-gap from the maxima of heavy hole band to the bottom of the conduction band at $k = 0$, the responsivity was increased by the applied electric field. Period of oscillation in the model qualitatively agrees with that in the experimental data. We calculated the Ge absorption coefficients from the responsivity spectra using Equation (3.1).

3.2.3 Absorption Coefficients Results

Figure 3.4 shows the absorption coefficients extracted from the spectral responsivity. As reflected in the responsivity spectra, the absorption coefficient was increased by the applied electric field for wavelengths longer than 1580 nm. At 1647 nm, at which we observed the largest field-induced absorption change, the applied electric field of 70 kV/cm significantly increased the absorption coefficient from 62 cm^{-1} to 230 cm^{-1}. This absorption increase is significant; therefore, we analyzed the absorption coefficient spectra using the generalized Franz-Keldysh formalism, which shows the dependence on the dielectric constant on an applied electric

field [28]. The change in dielectric constant ($\Delta\varepsilon$) at energy E under an applied electric field F can be expressed in terms of the electro-optic functions $G(\eta)$ and $F(\eta)$ as the following [26, 28]

$$\Delta\varepsilon(E,F) = (B/E^2)(\hbar\theta)^{1/2}[G(\eta) + iF(\eta)] \qquad (3.2).$$

where the parameter B is a constant for light- and heavy-hole transitions, respectively and is related to a material optical matrix element E_p. We used a value of E_p = 26.3 eV from the literature [34]. The parameters $\hbar\theta$ and η are calculated from the electric field magnitude, energy gap and reduced effective mass. We used the reduced effective mass for the light hole $\mu_{lh} = 0.0195m_0$ and the heavy hole $\mu_{hh} = 0.033m_0$. In our model, we considered the Franz-Keldysh (F-K) effect from the direct band edge. The contribution from the indirect band edge was ignored in this treatment.

3.2.4 Influence of Strain on the Franz-Keldysh Effect

We incorporated the strain effect into our Franz-Keldysh model. As the Ge films are under biaxial stress due to thermal expansion coefficient mismatch between the Ge films and Si substrates, the tensile strain in our Ge-on-Si films introduces the narrowing of Ge direct band gap and makes the light- and heavy-hole valence bands of Ge films become non-degenerate. The strained Ge films have two direct band-gaps from the maxima of light hole band and heavy hole band to the bottom of the conduction band at k = 0, as represented by E_g^{Γ}(lh) and E_g^{Γ}(hh), respectively [23-26]. In our model for the Ge films, we used E_g^{Γ}(lh) ~ 0.773 eV and E_g^{Γ}(hh) ~ 0.785 eV [26]. We assumed that the strain did not alter E_p and used E_p ~ 26.3 eV. We calculated the change in dielectric constant from light-hole energy-gap $\Delta\varepsilon(lh)$ and from heavy-hole energy gap $\Delta\varepsilon(hh)$ using the corresponding characteristics for each band gap. The sum of $\Delta\varepsilon(lh)$ and $\Delta\varepsilon(hh)$ results in total change in dielectric constant $\Delta\varepsilon$ from both light-and heavy-hole band transitions. The absorption coefficients α and refractive index n were calculated from the change in dielectric constant $\Delta\varepsilon$. Our model derives that the absorption coefficient at 1647 nm increases

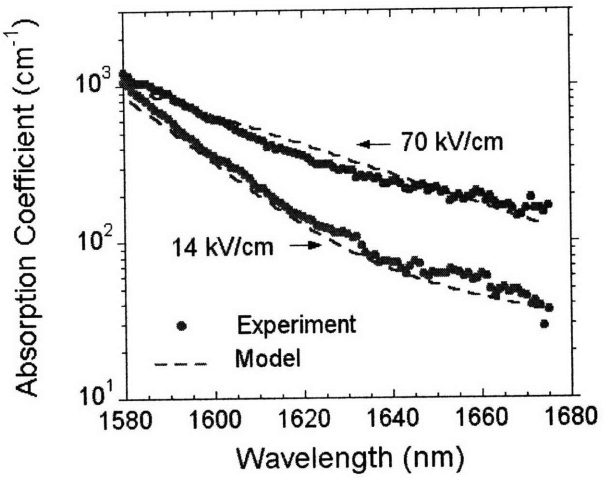

Figure 3.4 Excellent fit of experimental data to the model based on the generalized Franz-Keldysh formalism in the Equation (3.2) with the parameters E_g^{Γ}(lh) = 0.773 eV, E_g^{Γ}(hh) = 0.785 eV.

from 57 cm^{-1} to 230 cm^{-1} under 70 kV/cm, in a very good agreement with the experimental data as shown in Figure 3.4. The excellent fitting of the experimental data to the model suggests that the change in absorption coefficients is due to the electro-optic effect in the strained Ge films.

3.2.5 Predicted Figures-of-Merit of Ge-on-Si Modulator

For the purpose of estimating the electro-optic effect in our strained Ge films, we derived the figures of merit $\Delta n/F$ for phase modulator and $\Delta\alpha/\alpha$ for absorption modulators based on the experimental data. The ratio $\Delta n/F$ represents the change in real part of refractive index under an applied electric field. The ratio $\Delta\alpha/\alpha$ represents the normalized change in absorption coefficient. Figure 3.5 plots values of Δn and $\Delta\alpha/\alpha$ as a function of the applied electric fields F derived from our model at 1647 nm for our strained Ge films on Si substrates. The Δn curve shows a peak value at an applied field of 55kV/cm similar to the reported Δn curve in InGaAsP [29]. The slope of Δn vs. F indicates the maximum value of $\Delta n/F$ = 280 pm/V, in the same order of magnitude as that in InP [30] and $LiNbO_3$ [31] as shown in Table 3.1.

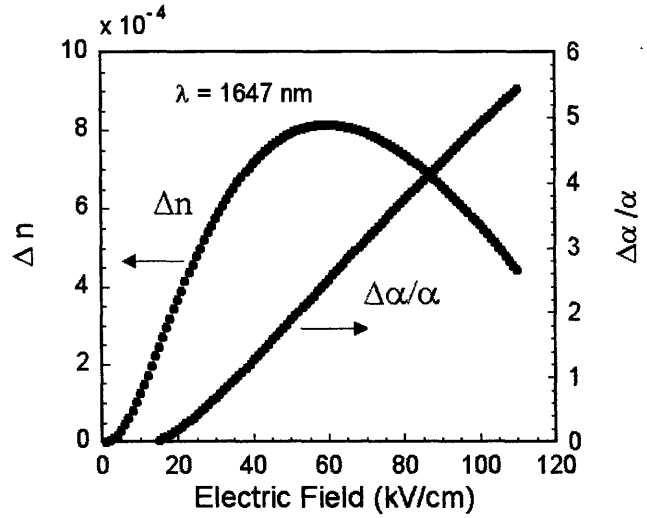

Figure 3.5 Application of the model to predict Δn and $\Delta\alpha/\alpha$ at 1647nm wavelength as a function of the applied electric field. The $\Delta n/F$ ratio for the strained Ge films on Si is 280 pm/V, comparable to those in InP and $LiNbO_3$.

For absorption modulator, the ratio $\Delta\alpha/\alpha$ represents optimized performance of the device with maximized contrast ratio and minimized insertion loss. As expected, $\Delta\alpha/\alpha$ increases with the applied electric field F. The ratio $\Delta\alpha/\alpha$ at F=70 kV/cm applied electric field has a value of 3.03, in a very good agreement with the measured value. This significant value of $\Delta\alpha/\alpha$ for the strained Ge film are equivalent to 7.5 dB contrast ratio and 2.5 dB material loss for a 100μm long optical absorption modulator. Our results show that the strained Ge films on Si substrates are very promising for efficient field-induced optical modulators.

Table 3.1 Summary of the electro-optic coefficients in strained Ge films on Si, Bulk Ge at 1647nm wavelength as being compared with those in InP [30] and $LiNbO_3$ [31].

	Strained Ge Films on Si	Bulk Ge	InP	$LiNbO_3$
$\Delta n/F$ (pm/V)	280	160	240	164

3.2.6 The Franz-Keldysh Effect in Ge-on-Si and Bulk Ge

We compared the values of $\Delta n/F$ and $\Delta\alpha/\alpha$ between our strained Ge films and bulk Ge. The ratios $\Delta n/F$ and $\Delta\alpha/\alpha$ for bulk Ge were calculated by substituting the direct bandgap E_g = 0.80 eV into our model. Table 3.1 shows the values of $\Delta n/F$ and $\Delta\alpha/\alpha$ under the applied field of 70 kV/cm for bulk Ge and our strained Ge films. The $\Delta n/F$ for bulk Ge is 160 pm/V, or about 60% of $\Delta n/F$ for our strained Ge films. The ratio of $\Delta\alpha/\alpha$ at 70 kV/cm for bulk Ge is 1.11, or about one-third of $\Delta\alpha/\alpha$ for our strained Ge films. At weakly absorbing regime, the presence of the tensile strain enhances the electro-optic effect in the Ge films by reducing the separation between the direct band gap, where the electro-optic effect is very strong as seen in the III-V materials, and the indirect band gap, where the material absorption is relatively weak. This finding is very important for optical modulator characteristics that require low insertion loss and large extinction ratio.

3.3 Design of Ge-on-Si Low- Loss Phase Modulator

Ge-on-Si shows a large ratio of $\Delta n/F$ at 1647 nm wavelength, giving Δn of ~ 8×10^{-4} under F=55 kV/cm; however, the material absorption of 62 cm^{-1} attributes to very high insertion loss. Since the material absorption is wavelength dependent, we determined an operation wavelength of Ge-on-Si phase modulator by calculating values of Δn as a function of wavelength. The generalized Franz-Keldysh formalism in section 3.2 was used to calculate the values of Δn under F=90 kV/cm. Figure 3.6 plots values of Δn as a function of wavelength. The curve of Δn shows oscillatory trend with the wavelength which is the characteristics of the Franz-Keldysh effect. Large value of Δn greater than 5×10^{-3} is observed near the direct bandgap. Value of Δn decreases in the area where is further from the direct bandgap.

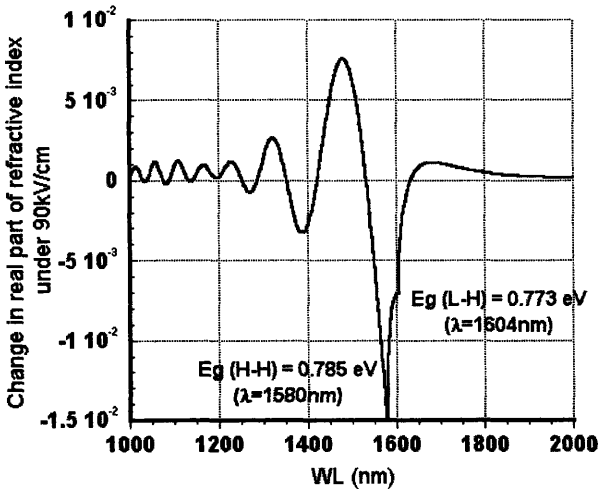

Figure 3.6 Variations in real part of refractive index under an applied electric field of 90 kV/cm.

To determine optimal wavelength for modulation, we plotted values of Δn and α with wavelength. Figure 3.7 shows value of calculated Δn and absorption coefficients α as a function of wavelength. Both Δn and α decreases with long wavelength. As in long wavelength or small photon energies, the effect from direct band gap gets smaller, resulting in decreasing values of Δn and α. We estimated the length of Mach-Zehnder (MZ) modulators and their insertion loss by using these values of Δn and α. For the modulator with single-arm operation, the length required for a π-phase shift L_π is given by [33]

$$L_\pi = \frac{\lambda}{2 \cdot \Gamma \cdot \Delta n} \tag{3.3}$$

where λ represents operation wavelength, Γ represents a confinement factor in SiGe waveguide. Insertion loss IL is expressed as

$$IL = 10\log\left(e^{-\alpha_{mod} L_\pi}\right) \tag{3.4}$$

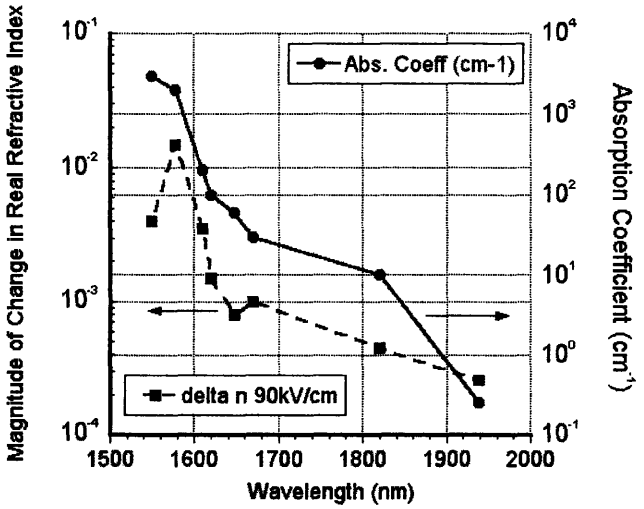

Figure 3.7 Values of calculated Δn under an applied electric field of 90 kV/cm and absorption coefficients α as a function of wavelength.

where α_{mode} is effective loss coefficient of the optical mode. The effective loss can be caused by material absorption of waveguide core, free carrier absorption in substrates or polysilicon electrodes. Value of parameters Γ and α_{mode} is subjective to the design of waveguide dimension.

To select the operation wavelength which yields low insertion loss, we plot values of L_π and insertion loss *IL* as a function of wavelengths in Figure 3.8. For the wavelength range between 1550 nm and 1620 nm, the length of the device L_π is shorter than 1 mm due to very large value of Δn; however, the insertion loss is still very high of > 10 dB due to large material absorption coefficients (> 100 cm^{-1}). To retain low insertion loss less than 3 dB, the operation wavelength that yields the best characteristics in Ge-on-Si phase modulator is at long wavelength (~ 1938 nm). Our model shows that the derived Δn under the electric field of 90 kV/cm at this wavelength is ~ 2.6×10^{-4}. Our model shows that Ge-on-Si Mach-Zehnder modulator works the best at long wavelength of ~ 1938 nm. The Ge Mach-Zehnder modulator with 3.8 mm long is predicted to give a π-phase shift with the electric field of 90 kV/cm. The insertion loss from

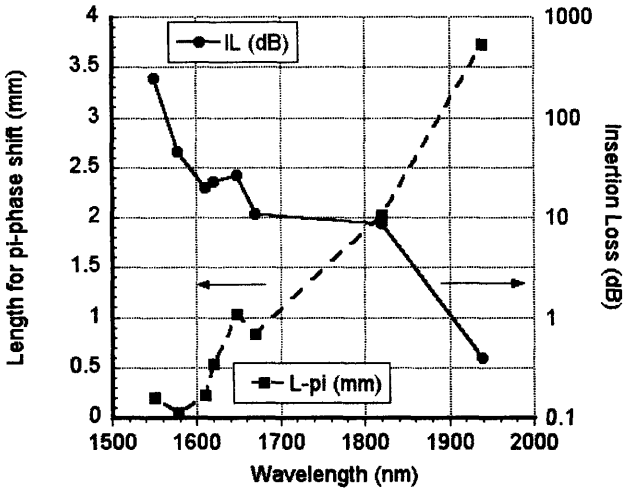

Figure 3.8 Required length of Mach-Zehnder modulators for a π-phase shift and insertion loss.

material absorption is approximately 0.4 dB.

3.4 Summary

Tensile Ge films on Si substrates demonstrate the strain-enhanced electro-optic effect in the weakly absorbing regime. The Ge films on Si substrates show strong electroabsorption effect at 1647 nm wavelength with normalized absorption change $\Delta\alpha/\alpha$ of ~ 3, in agreement with the Franz-Keldysh formalism. The derived electro-optic coefficient $\Delta n/F$ of Ge-on-Si is comparable to that of indium phosphide and lithium niobate. The results from the Franz-Keldysh model predict that Ge-on-Si phase modulators with 3.8 mm long phase shifter can reach a π-phase difference under a single-arm operation at 1938 nm wavelength. The predicted insertion loss is approximately 0.4 dB.

Chapter 4: Design of Franz-Keldysh-effect SiGe Waveguide Modulators

We present the design of SiGe electroabsorption and electro-optic modulators for 1550 nm wavelength applications using the Franz-Keldysh model. Our design covers material composition and device structure for each application. This chapter begins with background in optical property of Ge-rich SiGe and describes the design of electroabsorption and electro-optic modulators, respectively.

4.1 Background

Si_xGe_{1-x} alloys are indirect-bandgap materials. Si_xGe_{1-x} alloys with Si composition $x > 0.15$ have conduction band minimum at the X-point, a character that is similar to Si. On the other hand, Si_xGe_{1-x} alloys with Si composition $x \leq 0.15$ have the conduction band minimum at the L-point, a character that is similar to that in Ge [34-35]. This range of Si_xGe_{1-x} composition ($x \leq 0.15$) with the Ge-like characteristics is in our focus for the design of modulators. We utilized the Franz-Keldysh (F-K) model to calculate the change in real part of refractive index Δn and absorption coefficient $\Delta\alpha$ of Si_xGe_{1-x} alloys ($x \leq 0.15$) under the applied electric field F. We calculated values of Δn and $\Delta\alpha$ by substituting the effective mass m, the real part of the refractive index n, the direct bandgap E_g^{Γ} and the optical transition matrix element E_P of Si_xGe_{1-x} alloys into the Franz-Keldysh model. Only the effective mass is independent of the alloy composition. We assumed that the effective mass of electron and hole in Si_xGe_{1-x} alloys ($x \leq 0.15$) is the same as that in Ge. Value of E_g^{Γ} and n in Si_xGe_{1-x} is linearly interpolated between Ge and Si. Real part of refractive index n of Si_xGe_{1-x} alloys ($x \leq 0.15$) at 1550nm is $4.10-0.64x$ [34-35]. The direct bandgap at room temperature is $(0.8+3.26x)$ eV [34-35].

Other parameters were affected by the composition and the tensile strain intrinsic to the films. Due to similar thermal expansion coefficient of Ge-rich SiGe to Ge, the SiGe films were assumed under tensile strain of 0.2%. The deformation potential theory was used to calculate the bandgaps from the maxima of light hole, heavy hole and split-off bands to minima of the Γ valley $E_g^{\Gamma}(lh)$ $E_g^{\Gamma}(hh)$ and $E_g^{\Gamma}(so)$. The deformation potential, elastic constants and split-off energy are linearly interpolated between Ge and Si. The optical transition matrix element E_P is calculated by using a following equation [29]

$$E_P = \frac{3(\frac{m_0}{m_e} + 1)}{\frac{1}{E_g^{\Gamma}(lh)} + \frac{1}{E_g^{\Gamma}(hh)} + \frac{1}{E_g^{\Gamma}(so)}} \tag{4.1}$$

These parameters were substituted into the generalized Franz-Keldysh formalism to estimate the electro-optic effect in Ge-rich SiGe material.

4.2 Design of Electroabsorption Modulators

Electroabsorption (EA) modulators are one of the best candidates for integrated modulators due to their small footprint, power dissipation and strong extinction ratio. Efficiency of EA modulators is evaluated by contrast ratio $\Delta\alpha/\alpha$, which represents normalized extinction ratio to insertion loss. Tensile-strained Ge films on Si substrates show a value of ~ 3 for a contrast ratio at 1647 nm wavelength [36]. To shift the modulation wavelength to 1550 nm, the direct bandgap needs to be reduced by adding Si into Ge [37]. The Franz-Keldysh model was used to estimate the optimal Si_xGe_{1-x} composition. We calculated values of $\Delta\alpha/\alpha$ under F = 100 kV/cm and 10 kV/cm for various compositions. Figure 4.1 plots value of $\Delta\alpha/\alpha$ as a function of wavelength for various Si compositions from 0.5% to 1.1% Si. The optimal composition is around 0.75% Si, or $Si_{0.0075}Ge_{0.9925}$, giving an absorption contrast $\Delta\alpha/\alpha$ of ~ 3. Due to the relatively high absorption coefficient (158 cm^{-1}), the length of the EA modulator should be less than 70 μm for an insertion loss of 5 dB.

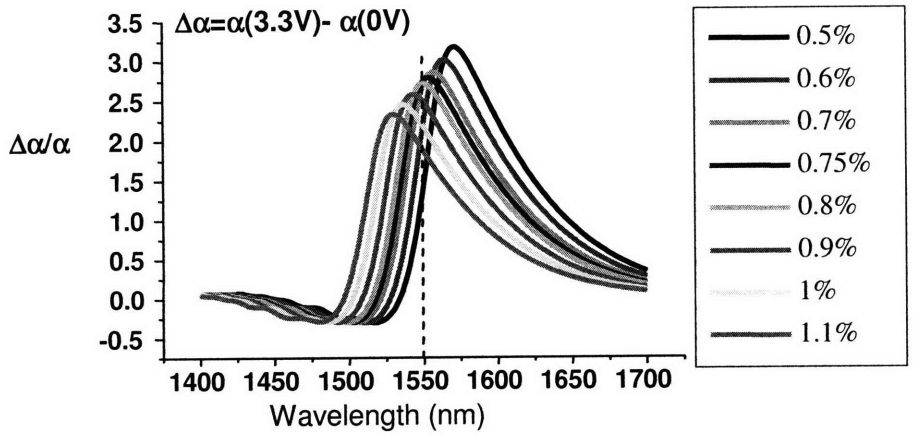

Figure 4.1 Normalized change of absorption as a function of wavelength for a range of Si composition from 0.5 to 1.1% Si. Courtesy of Dr. Jifeng Liu.

Because of very short SiGe waveguide, the EA modulator needs Si waveguide butt-coupling for optical input and output [37]. Bandwidth, extinction ratio and insertion loss of the EA modulators was calculated. Figure 4.2 shows the bandwidth, extinction ratio and insertion loss as a function of device length for $Si_{0.0075}Ge_{0.9925}$ EA modulator with 600 nm in width and 400 nm in height. We assumed 50×50 μm^2 metal contact pads with the load resistance of 50 Ω and vertical distance of 4 μm from substrate, so the pad capacitance was 21.6 fF. For a 50 μm long SiGe modulator, we predicted an extinction ratio of 10 dB and a 3 dB bandwidth of > 50 GHz.

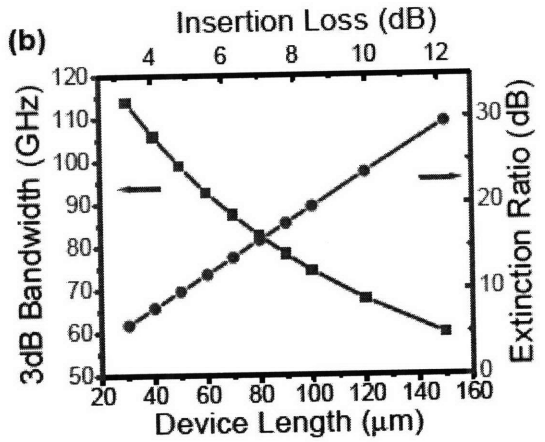

Figure 4.2 Bandwidth, insertion loss and extinction ratio as a function of device length [37]. Courtesy of Dr. Jifeng Liu.

4.3 Design of Mach-Zehnder modulators

Mach-Zehnder structures are widely used to implement optical intensity modulation. Figure 4.3 shows a schematic diagram of Mach-Zehnder modulator with a single arm of electro-optic waveguide. Mach-Zehnder structures consist of an input port, a splitter that divides the input optical power into two equal portions, two waveguides and another splitter that merges light from the two waveguides into an output port. One of the waveguides in the interferometer is designed with electrical electrode, along which the optical phase can be modulated by an applied voltage *V*.

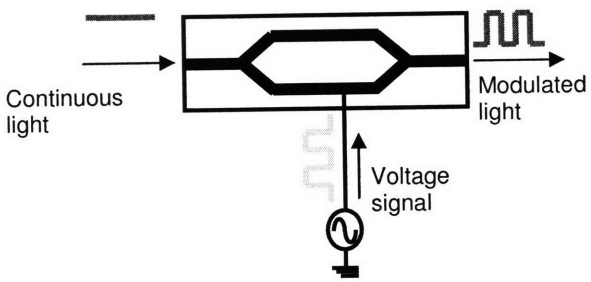

Figure 4.3 A schematic diagram of Mach-Zehnder Interferometer with single-arm operation.

The applied voltage induces the phase difference of light in the two arms. If the two beams are in phase after propagating along the two waveguides, they constructively interfere, which results in a maximum intensity output. On the other hand, if the optical waves are out of phase or reach a π-phase difference, they destructively interfere, which results in a minimum intensity. By applying voltage, we can modulate the light output from Mach-Zehnder modulators. For a single-arm operation, phase difference $\Delta\Phi$ relates to change in the real refractive index of core material by a following expression [33]:

$$\Delta\Phi = \Gamma \cdot \Delta n \cdot \frac{2\pi}{\lambda} L \tag{4.2}$$

where Γ is a confinement factor of optical mode in the SiGe core of waveguides, λ is operation wavelength and L is length of phase shifter. To maximize value of $\Delta\Phi$ without sacrificing compact device, we should design waveguide dimension to maximize product of $\Gamma \cdot \Delta n$. Value of Δn is dependent on an applied electric field F, which is inversely proportional to the core thickness under a constant applied voltage V. On the other hand, Γ is also dependent on thickness and width of waveguides. Correlation of Γ and core dimension is more complicated and requires mode solver calculation. To achieve a design of efficient modulator, we considered both material and device design.

4.4 Material Design of Mach-Zehnder modulators

The optimal wavelength for phase modulation in Ge-on-Si is nearly 2000 nm wavelength, which corresponds to 0.64 eV. The separation between the operation energy and the direct bandgap is called detuning energy and has value of ~ 0.13 eV in Ge-on-Si. We first attempted to determine the composition of Si_xGe_{1-x} for modulation at 1550 nm (or at 0.80 eV), by applying the same value of detuning energy (~ 0.13 eV) to determine the direct bandgap of Si_xGe_{1-x} for modulation at 1550 nm (or at 0.80 eV). The calculation shows that $Si_{0.045}Ge_{0.955}$ with the direct gap of ~ 0.93 eV will yield optimal phase modulation at 0.80 eV. The change in the real part of

refractive index Δn in $Si_{0.045}Ge_{0.955}$ under F=100 kV/cm was calculated by using the F-K model (Equation 3.2) and the parameters discussed in section 4.1. Figure 4.4 shows (a) the absorption coefficient and (b) calculated value of Δn in $Si_{0.045}Ge_{0.955}$ as a function of photon energy. Value of Δn at 1550 nm was ~ 2×10^{-4}, comparable to Δn of Ge at nearly 2000 nm. The value of Δn was substituted into Equation (3.3) to calculate the length for a π-phase shift L_π, which gave L_π of ~ 3.9 mm. The corresponding insertion loss was 72 dB due to high absorption from the indirect-bandgap transition. This high insertion loss made $Si_{0.045}Ge_{0.955}$ not applicable for modulator applications at 1550 nm wavelength.

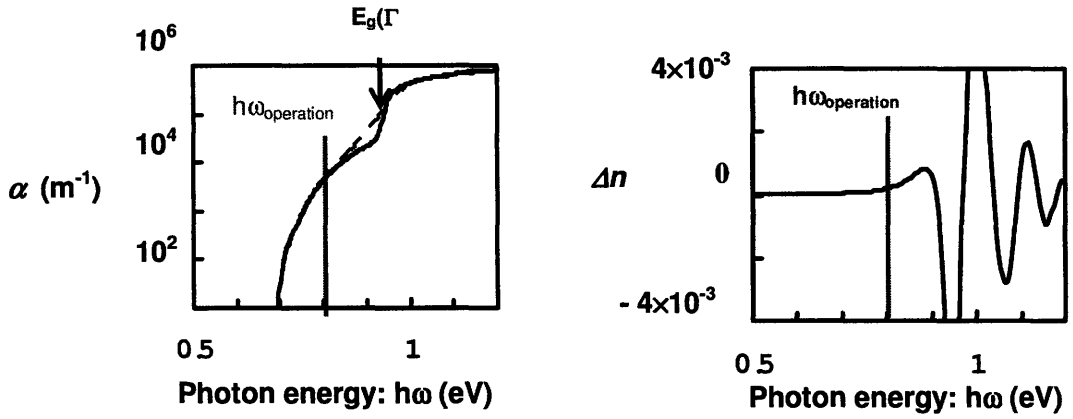

(a) (b)

Figure 4.4 Absorption coefficient of $Si_{0.045}Ge_{0.955}$ and change in real part of refractive index under an applied field of 100 kV/cm as a function of photon energy. Courtesy of Suguru Akiyama.

Since one of important factors for phase modulator is low insertion loss, we determined the Si_xGe_{1-x} composition that gave low absorption coefficient by calculating values of α and n as a function of composition. Figure 4.5 (a) plots value of Δn and α at 1550nm as a function of Si composition. For SiGe with Si composition less than 4%, the value of Δn was greater than 4×10^{-4}. However, the absorption coefficient α was greater than 50 cm^{-1}. As Si was added into Ge, value of both of Δn and α reduced. When Si composition reached approximately 11%, value of Δn and

α reduced to 2×10^{-5} and 1 cm^{-1}, respectively. This trend shows a correlation between Δn and α on Si composition. Material composition of $Si_{0.135}Ge_{0.865}$ was chosen for phase modulator applications due to its low absorption coefficient of 0.1 cm^{-1} at 1550 nm wavelength. Value of Δn was derived using the F-K model and material parameters for SiGe discussed in section 4.1. The derived Δn of $Si_{0.135}Ge_{0.865}$ is 1.2×10^{-5} under the applied electric field of 100kV/cm. We calculated value of L_π and insertion loss by substituting Δn into Equation (3.3) and (3.4). Figure 4.5 plots L_π and insertion loss as a function of Si composition. Value of L_π increased with Si composition. On the other hand, insertion loss decreased with Si composition. Value of Δn in $Si_{0.135}Ge_{0.865}$ was ~ 1.2×10^{-5}, giving L_π of 66 mm and insertion loss of 5.4 dB.

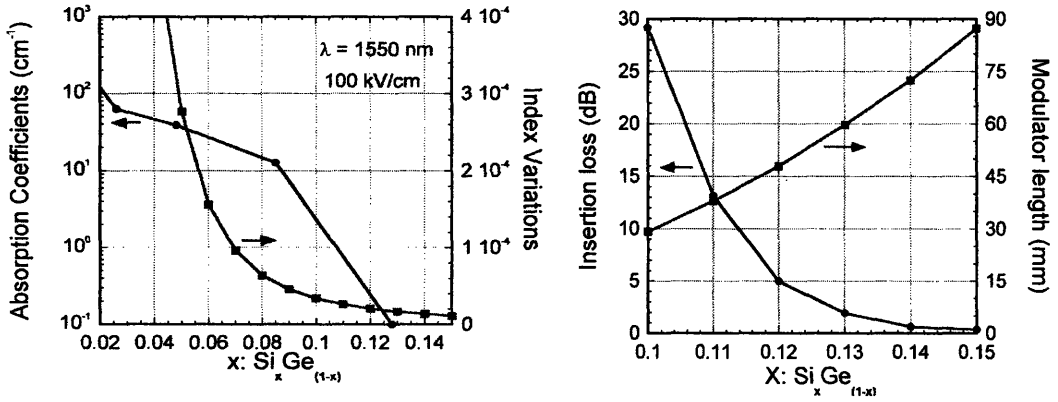

(a) (b)

Figure 4.5 (a) absorption coefficient and change in the real part of refractive index under an applied field of 100 kV/cm and (b) insertion loss and modulator length as a function of Si content in SiGe.

4.5 Device Design of Mach-Zehnder modulators

The dimensions of rib waveguide were designed to optimize the overlapping between optical mode and the electric field distribution. The rib waveguides provide large optical mode and an ease of coupling. The optical mode was mostly confined in SiGe core, where existed high electric field to induce Δn. Figure 4.6 illustrates the cross-sectional diagram of the SiGe rib waveguide with oxide top cladding. The substrate and polysilicon electrode were heavily doped to ensure high electric field across the SiGe waveguide core. We assumed value of n and α in p-type, boron-doped Si substrate was 3.46 and 10 cm^{-1}, respectively. The same value of n and α was assumed in n-type, phosphorus-doped polysilicon as well. Apollo photonics mode solver was used to calculate the confinement factor Γ. The width of SiGe rib was 1 μm. The rib height was 0.1 μm. Total thickness of SiGe layer d was 0.5 μm.

The calculation yielded a value of $\Gamma \sim 0.786$. The change in the real part of effective index Δn_{eff} was equal to a product of Γ and Δn, giving a value of $\Delta n_{eff} \sim 9.4 \times 10^{-6}$. Derived value of L_π was ~ 84 mm with the insertion loss of ~ 35 dB. Again, we encountered the issue of high insertion loss. In the design, insertion loss was attempted to reduce by optimizing waveguide dimensions, modifying doping profile in Si substrates and polysilicon electrodes, and designing the dual-arm operation.

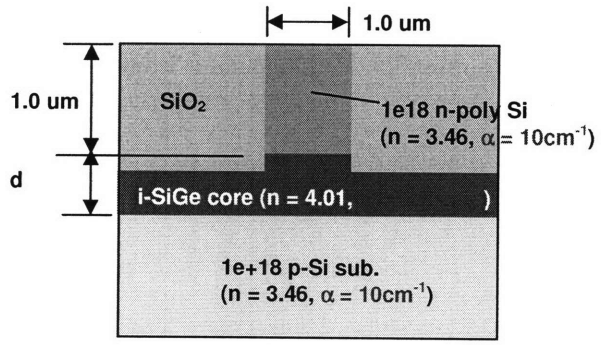

Figure 4.6 SiGe rib waveguide structure.

4.5.1 Core thickness optimization

We determined the optimal value of the core thickness by plotting device length and insertion loss as a function of the thickness. Value of Δn under the applied electric field F was calculated by assuming a constant voltage of 5 V applied to the SiGe waveguide. In our design, we optimized waveguide thickness d by keeping a fixed waveguide width at 1 μm, and calculated value of Δn under the applied field $F = V/d$, and corresponding confinement factor Γ. The change in real part of effective index was calculated by a product of Δn and Γ. Figure 4.7 (a) shows the index variation Δn and device length L_π as a function of the thickness. Value of Δn was inversely proportional to the SiGe thickness d. Therefore, the device length L_π increased with increasing SiGe thickness.

To estimate optical loss in SiGe waveguide, we calculated confinement factor as a function of the thickness. Figure 4.7 (b) shows that the thickness of 0.5 μm yielded the highest confinement factor, which was desirable for the possible largest value of Δn_{eff}. The insertion loss was calculated by taking the confinement factor Γ and device length L_π into account (Equation 3.4). The thickness of 0.25 μm and 0.5 μm gave similar insertion loss when the thickness of 1 μm yielded the highest insertion loss due to increasing device length. This suggests that the thickness of 0.5 μm results in the optimized insertion loss and device length. The design shows that the thickness of 0.5 μm is optimal thickness for SiGe rib waveguide modulators.

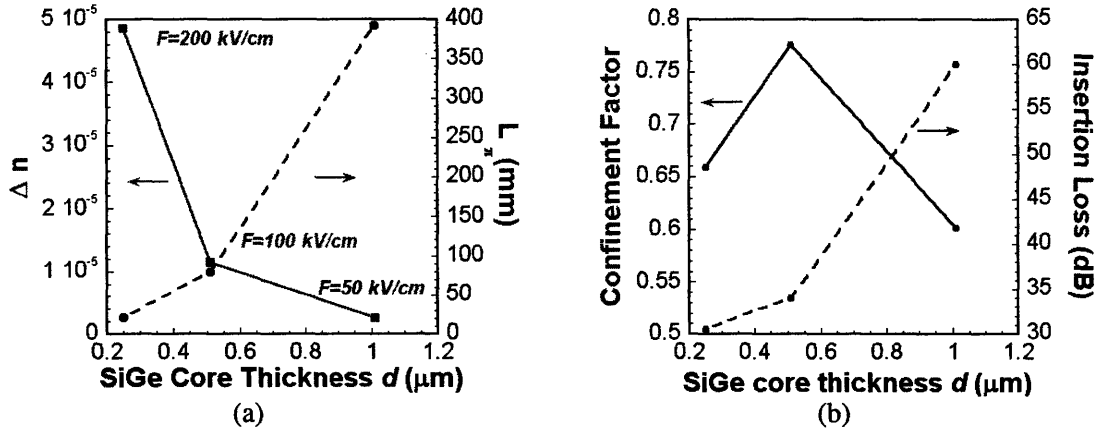

Figure 4.7 (a) Calculated change in real part of refractive index of $Si_{0.135}Ge_{0.865}$ under an applied voltage of 5 V and device length required for a π phase shift as a function of the core thickness. (b) Calculated confinement factor and insertion loss as a function of the core thickness.

4.5.2 Doping Profile Modification

Optical loss in SiGe waveguide could be reduced by inserting a lightly boron-doped layer underneath and another lightly phosphorus-doped layer above the SiGe film. In the design, a 0.1 μm thick, lightly boron-doped layer and a 0.1 μm thick, lightly phosphorus-doped layer with carrier concentrations of 1×10^{17} cm^{-3} were assumed. Each layer was assumed with the absorption of 1 cm^{-1}. Figure 4.8 shows a schematic diagram of cross-section of (a) the original and (b) the modified SiGe waveguides with inserted lightly doped layers. Under an applied voltage of 5 V, the strength of electric field reduced from 100 kV/cm to 85 kV/cm across a 0.5μm thick SiGe layer. Value of Δn reduced to 6.9×10^{-6} and of α_{mode} was 0.44 cm^{-1}. Due to a reduction in value of Δn and α_{mode}, the device length for a π-phase shift L_π became 113 mm, and the insertion loss reduced to 21 dB.

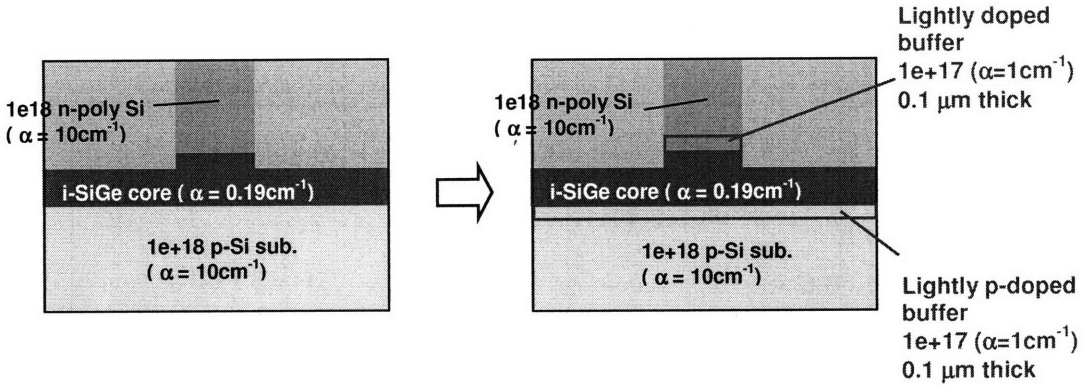

(a) (b)

Figure 4.8 Schematic cross-section of (a) the original and (b) modified SiGe waveguides.

4.5.3 Dual-Arm Operation

The length of phase shifter and insertion loss was reduced by changing operation mode to dual-arm operation, which voltage-dependent phase delay was introduced in both arms. We designed phase shifter of 15 mm long which exhibited insertion loss of 3 dB. We predicted that this device could reach a π-phase shift by using a dual-arm operation with the applied voltage of 10 V on each arm. For an AC operation we anticipated that this device could reach 0.27 π phase difference. The transfer function of this device was calculated by using the expression [32,37]:

$$T = \frac{1}{2}\left[1 + \cos\left(\Delta\Phi(V)\right)\right] \tag{4.3}$$

where T represents normalized output power. Figure 4.9 shows the normalized output power as a function of phase shift. We predicted that the applied voltage of 5 V under an AC operation gave 3.7 dB extinction ratio with additional insertion loss of 1.5 dB.

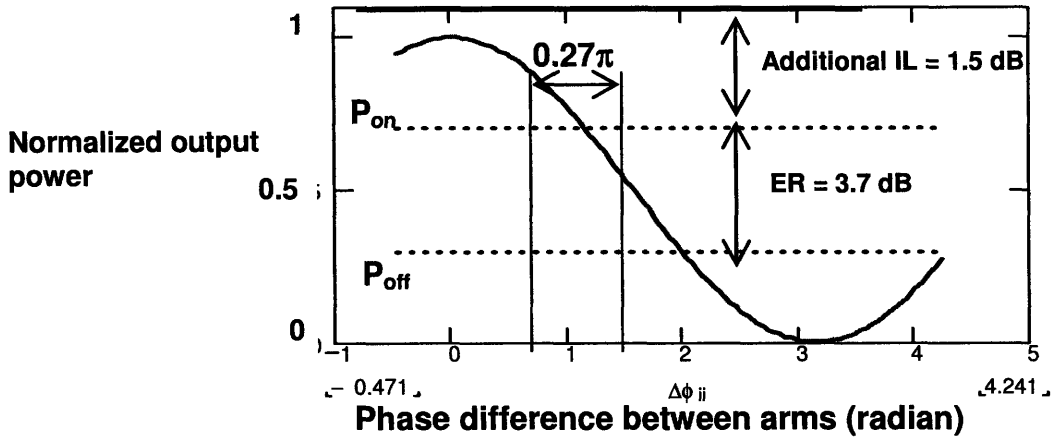

Figure 4.9 Calculated normalized transmission of SiGe Mach-Zehnder modulators under dual-arm operation. Courtesy of Suguru Akiyama.

4.6 Summary

We present the design of the electric-field-effect electroabsorption and electro-optic modulators. To shift the operation wavelength to 1550 nm, Si is added into Ge to shift the energy gap. SiGe with Si composition of ~ 0.75% Si is optimal composition for electroabsorption modulators. Our calculation shows that a 50 μm long SiGe modulator yields an extinction ratio of 10 dB and a 3 dB bandwidth of > 50 GHz. SiGe with 13.5% Si is optimal composition for the electro-optic modulators. The waveguide dimensions and doping profiles were optimized to reduce the insertion loss. We predict that Mach-Zehnder modulator with two phase shifters of 15 mm long will yield an extinction ratio of 3.7 dB with additional insertion loss of 1.5 dB.

Chapter 5: Direct Epitaxial Growth of SiGe epilayer on Si for Phase Modulator Applications

Realization of the field-effect SiGe modulators for 1550 nm application requires deposition of Ge-rich SiGe films on Si substrates. This chapter describes the experiments of Ge-rich Si_xGe_{1-x} deposition on Si substrates using ultrahigh vacuum chemical-vapor deposition (UHV-CVD) systems, and discusses the experimental findings. Section 5.1 provides the prior work in SiGe heteroepitaxial deposition. In our experiments, we chose to deposit Ge-rich SiGe films using two-step growth process, similar to the two-step Ge growth. Section 5.2 discusses the motivation of developing low-temperature SiGe buffer deposition. Section 5.3 describes the experiments and kinetic model of the low-temperature SiGe buffer deposition. Section 5.4 discusses high-temperature SiGe deposition, growth rate and film property.

5.1 Prior Developments in SiGe/Si Heteroepitaxial Deposition

High-quality SiGe and Ge heteroepitaxy deposition has been significant technology development since the deposition provides an opportunity to engineer band structure for improved device performance [39-42]. Structural similarity in Si and Ge provides miscibility in Si_xGe_{1-x} alloys, providing solid solutions over the entire composition range. Challenge in heteroepitaxial deposition of Ge films on Si substrates lies in the lattice mismatch of ~ 4.2% introduces misfit strain. As films grow thicker, the strain energy must be relaxed via coherent surface undulation (elastic relaxation) or introduction of misfit dislocation (plastic relaxation) [43-46]. The strain causes surface corrugation while keeping coherent films. Misfit dislocations can also be introduced to relieve the strain energy of an elastically strained layer [46]. Since the dislocations cannot end within the bulk, they must terminate on the edge or surface of the films or close upon themselves by forming a closed loop [43-46]. Some misfit dislocations propagate along (111) planes to the film surface; these dislocations are so called threading dislocations. The

threading dislocations introduce the midgap states that reduce carrier lifetime and are deleterious for device performance [47].

Chemical vapor deposition (CVD) technique of Si_xGe_{1-x} layers on Si substrates has been developed in an attempt to reduce dislocation density. Deposition of SiGe buffer layers are used to deposit high-quality SiGe films [48-54]. Fitzgerald et al demonstrate the first effective compositionally graded buffers [48]. The graded buffers were deposited at high temperature, yielding fully relaxed buffer, which accommodate strain relieved by existing misfit dislocations. By this way, nucleation of new dislocation is suppressed. At the deposition temperature (750-900°C), the dislocations can glide very fast, enabling effective removal of dislocations out of the films. They improved the buffer growth and increased the final composition of the buffer. Above 50% Ge composition, the strain introduces surface undulation, which introduces dislocation pile-up and prevents further relaxation by grading. To remove the surface roughness, they interrupted the growth and use chemical-mechanical-polisher (CMP) to flatten the surface. The growth was resumed and continued of compositional grading for Ge films. A grading rate of 10%Ge μm^{-1} is used with a 2 μm Ge cap for a total thickness of 12 μm. This process yields a threading dislocation density of 2.1×10^{-6} cm^{-2}.

Another heteroepitaxy deposition technique has been developed by using constant-composition buffer or so called two-step deposition technique. This technique was first developed for Ge deposition on Si substrates. The buffer with composition matched to the films was deposited at low temperature ($T<$ 400°C). Despite large lattice mismatch, the buffer deposited at this temperature is planar due to limited surface-diffusion, which prevents surface islanding [61]. The remainders of the films are deposited at high temperature, and the deposition is followed by thermal annealing [53]. Upon cooling, tensile strain is accumulated in Ge films since the expansion coefficient of Ge is larger than that of Si. Thermally induced strain, which is caused by the mismatch of thermal expansion coefficient between SiGe films and Si substrates,

induces the dislocation glide, increasing a probability of dislocation annihilation and yielding a reduction in dislocation density. Annealing of the Ge films reduces the dislocation density to $2\times10^{7}cm^{-2}$ [53]. *p-i-n* diodes fabricated from the annealed Ge films demonstrate rectifying I-V characteristics and spectral responsivity [27, 55]. Ge-rich Si_xGe_{1-x} ($0 \leq x \leq 0.053$) films deposited on Ge buffers using the two-step UHV-CVD growth process demonstrate film quality comparable to the similarly grown Ge films [56-57]. Etch-pit-density shows threading dislocation density of ~ 2-3 $\times$ 10^{7} cm^{-2} in annealed SiGe films, comparable to that in Ge films. The data suggest that alloying small amount of Si in Si_xGe_{1-x} with $x \leq 0.053$ does not inhibit dislocation motion [56-57]. Since the optimal composition for phase modulators is $Si_{0.135}Ge_{0.865}$, the deposition of Ge-rich Si_xGe_{1-x} for x ~ 0.135 was investigated.

5.2 Ge-rich SiGe films on Ge buffers

5.2.1 Experimental Procedure

Si_xGe_{1-x} ($0 \leq x \leq 0.108$) films were deposited on Si substrates using the two-step deposition technique in the UHV-CVD system. Prior to loading the wafers into the UHV-CVD reactor, the wafers were cleaned by Piranha solution (H_2SO_4:H_2O_2=3:1) for 10 minutes and followed by de-ionized water (DI) rinse. The wafers were carefully dipped in HF solution (HF:H_2O=1:5) for 30 seconds to passivate the substrate surface with hydrogen. The wafers were loaded into the reactor at the deposition temperature. Diluted germane (GeH_4) in Ar gas (35% GeH_4) was used as a gas source to deposit Ge buffer at 335°C. Then, the temperature was raised to 700°C or 800°C. At the elevated temperature of $\geq$ 700°C, Si_xGe_{1-x} ($0 \leq x \leq 0.108$) films were deposited by using germane and silane (SiH_4) as gas sources. Film composition was characterized by X-Ray Diffraction technique. Atomic Force Microscopy (AFM) was used to study the surface topography of 1 μm thick Ge and SiGe films. Table 1 summarizes growth parameters and film characteristics for SiGe films deposited on Ge buffer. At fixed 10 sccm GeH_4 and 3 sccm SiH_4 flow, more Si content was incorporated into alloy films with increasing growth temperature.

Table 5.1 growth parameters and film characteristics for SiGe films deposited on Ge buffer.

Sample	T (°C)	GeH_4 (sccm)	SiH_4 (sccm)	x_{Si} (%)	Surface roughness (nm in rms)
R596	700	10	-	0	~ 0.5
R601	700	10	3	10.7	~ 10.6
R602	800	10	3	14.2	~ 14

5.2.2 Results and Discussion

Figure 5.1 (a)-(d) show the AFM images of (a) Ge, (b) $Si_{0.0076}Ge_{0.9924}$, (c) $Si_{0.02}Ge_{0.98}$ and (d) $Si_{0.11}Ge_{0.89}$ films deposited on Ge buffers. The surface of Ge film in Figure 5.1 (a) is very smooth with the roughness of ~ 0.5 nm in root-mean-square (rms). With addition of Si into SiGe films, the surfaces became more undulating. Figure 5.1 (d) shows very rough surface of $Si_{0.107}Ge_{0.893}$ film with the roughness of ~ 10.6 nm in rms. Increasing surface roughness with Si composition in SiGe films was caused by the lattice mismatch between the Ge buffers and the remainders of the SiGe films. The lattice mismatch introduced strain energy in the films, causing surface undulation.

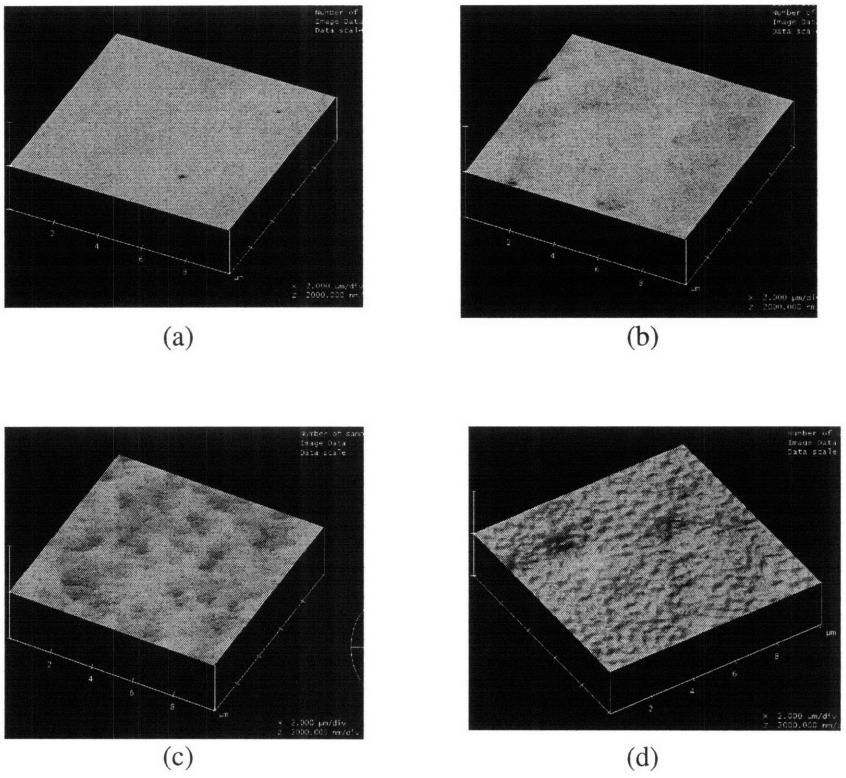

Figure 5.1 AFM images of (a) Ge, (b) Si $_{0.0076}$Ge $_{0.9924,}$ (c) Si $_{0.02}Ge_{0.98}$ and (d) Si $_{0.11}Ge_{0.89}$ deposited on Ge buffers/Si substrates.

Mechanism of strain relaxation via surface undulation is described as following. In an attempt to relieve the misfit strain, fluxes of atoms diffuse away from stress-concentrated area near the interface to the relaxed surface. Figure 5.2 shows schematic cross section of undulating surface. The arrows represent the directions of the atomic flux away from the cusp valley at which high stress concentration accumulates. The flux of atoms diffuses towards the peak, where the stress is relieved, resulting in surface undulation. The formation of the surface undulation reduces strain energy ε in the layers with an expense of increasing surface energy γ. Therefore, periodicity of the undulating surface is constrained by a minimum thermodynamically stable wavelength λ_{cr} [58-59]:

$$\lambda_{cr} = \frac{\gamma}{\varepsilon^2} \qquad (5.1).$$

Roughened surface is undesirable film quality for planar processing. The roughened surface with high stress concentration at the valley may also promote the nucleation of dislocations or can block the dislocation glide [50]. By reducing the misfit strain between the buffer and the remainder of the film, surface morphology of SiGe films can be improved. To make surface planar, deposition of buffer layer with composition matched to remainder of the films should decrease misfit strain. Deposition of SiGe buffer at low temperature is discussed in Section 5.3.

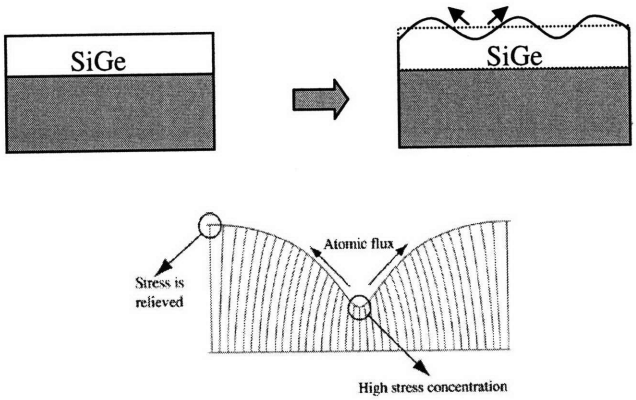

Figure 5.2 Surface undulation and schematic view of stress concentration in undulating surface [59].

5.3 Low-Temperature Ge-rich SiGe Buffer Deposition

5.3.1 Experimental Procedure

Epitaxial Si_xGe_{1-x} layers were deposited on 6" p-type Si(100) wafers at 360°C using 100% SiH_4 and GeH_4 source gases in a commercial (Unaxis) hot-wall UHV-CVD reactor. The base pressure was ~ 10^{-9} mTorr at 650°C. Prior to loading, the wafers were cleaned by standard RCA and dipped in 50:1 HF solution for 30 seconds, after which the wafers went through DI water rinse and spin dry. The wafers were in-situ annealed at 780°C for 20 minutes under H_2 ambient to remove residual oxide. Then, the reactor was cooled to 360°C under H_2 ambient and SiH_4 and GeH_4 started to flow. In each deposition, we aimed at a different Si_xGe_{1-x} film composition by varying SiH_4 flows (0.5, 1, 2 and 6.8 sccm) while keeping the GeH_4 flow constant (at 10 sccm). Processing pressure varied from ~ 14 mTorr to ~ 20 mTorr, depending on total gas flow in the reactor. SiGe film composition and single-crystal quality was determined by X-Ray Diffraction technique (XRD), and film thickness was determined by selective etch and profilometer. Our Si_xGe_{1-x} films grown at 360°C are Ge-rich SiGe with Si composition, x, up to 12.3%. Four films were studied with various composition and growth rates as shown in Table 5.2. In all cases, the flow of GeH_4 kept constant at 10 sccm.

Table 5.2 Film property (silicon composition x and film growth rate R_{SiGe}) and deposition parameter (GeH_4 flow, SiH_4 flow and total pressure).

x in Si_xGe_{1-x}	GeH_4 flow (sccm)	SiH_4 flow (sccm)	Total Pressure (mTorr)	Growth rate R_{SiGe} (A/hour)
0.8%	10	0.5	14.1	552
1.9%	10	1	14.6	434
3.6%	10	2	15.5	329
12.3%	10	6.8	20.0	264

The Si composition x in Si_xGe_{1-x} films and the corresponding film growth rates R_{SiGe} are plotted as a function of SiH_4 flow and the constant GeH_4 flow in Figure 5.3. The Si composition x increased linearly with the SiH_4 flow. However, the film's growth rate decreased with the increasing SiH_4 flow. Kinetic models were developed to explain this growth behavior of SiGe buffer.

5.3.2 Growth Model

Chemical Vapor Deposition (CVD) of SiGe from SiH_4 and GeH_4 combines a series of reactions. The total chemical vapor deposition of Si_xGe_{1-x} is:

$$SiH_4(g) \rightarrow 2H_2(g) + \underline{Si} \tag{5.2}$$

$$GeH_4(g) \rightarrow 2H_2(g) + \underline{Ge} \tag{5.3}$$

An initial step for the CVD process is the adsorption of SiH_4 or GeH_4 molecules and their decomposition into SiH_3 or GeH_3 and H [60-61]. The adsorption reaction for each SiH_4 or GeH_4 molecule requires two free surface sites as followings:

$$SiH_4(g) + 2\_ \rightarrow \underline{SiH_3} + \underline{H} \tag{5.4}$$

$$GeH_4(g) + 2\_ \rightarrow \underline{GeH_3} + \underline{H} \tag{5.5}$$

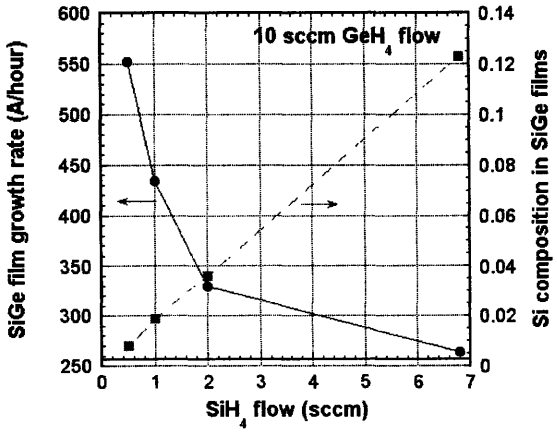

Figure 5.3 Growth rates and Si composition in SiGe films as functions of SiH_4 flow (GeH_4 flow kept constant at 10 sccm, growth temperature is 360°C for all films).

$\underline{SiH_3}$, $\underline{GeH_3}$ and $\underline{H}$ represent gas species attached to surface sites. Free surface sites available for the adsorption reactions are represented by _. The free sites are released only when H_2 molecules desorb off the surface in a following reaction [60]:

$$2\underline{H} \rightarrow H_2(g) + 2\_ \tag{5.6}$$

Since the adsorption reactions (reactions 5.4 and 5.5) can happen on the free sites, the H_2 desorption (reaction 5.6) is one of the factors that determines the growth rate.

5.3.3 Growth rate

The growth rate, R_{SiGe}, for Si_xGe_{1-x} is the sum of the growth rate of Si , R_{Si} and Ge, R_{Ge}:

$$R_{SiGe}(x) = R_{Si}(x) + R_{Ge}(x) \tag{5.7}$$

Values of R_{Si} and R_{Ge} were calculated from experimental growth rate using $R_{Si}=xR_{SiGe}$ and $R_{Ge}=(1-x)R_{SiGe}$. We assumed that the SiGe deposition at 360°C is in the surface reaction limited regime [62]. R_{Si} and R_{Ge} relate to partial pressure of SiH_4 P_{SiH4} and GeH_4 P_{GeH4} respectively. R_{Si} and R_{Ge} can be expressed as:

$$R_{Si} = k_{Si}(1-\theta)^2 P_{SiH4} \tag{5.8}$$

$$R_{Ge} = k_{Ge}(1-\theta)^2 P_{GeH4} \tag{5.9}$$

where k_{Si} and k_{Ge} represent surface reaction rate constants for SiH_4 adsorption and GeH_4 adsorption reactions, respectively. A fraction of the free surface sites is represented by $(1-\theta)$. The fraction is squared in the expression for the growth rate to account for the fact that each SiH_4 or GeH_4 molecule requires two free surface sites for adsorption. We obtained the growth rate expressions in unit of [cm/second] from the Equations (5.8)-(5.9) by replacing gaseous pressure P_{SiH4} and P_{GeH4} with material density D [g/cm^3], molecular weight M [g/mol] and flux J [molecules/cm^2-second] [63]. The derived expression for the growth rate is as follows:

$$R_{Si} = \frac{J_{SiH4} M_{Si}}{D_{Si} N_A} k_{Si}(1-\theta)^2 \tag{5.10}$$

$$R_{Ge} = \frac{J_{GeH4} M_{Ge}}{D_{Ge} N_A} k_{Ge} (1-\theta)^2 \tag{5.11}$$

where N_A is Avogadro's number, the value of Si density D_{Si} is 2.3296 g/cm^3 and Ge density D_{Ge} is 5.3234 g/cm^3. Si molecular weight M_{Si} is 28.086 g/mol and Ge molecular weight M_{Ge} is 72.64 g/mol [64]. We assumed molecular flow regime during deposition; therefore, the flux J to the surface is dependent on partial pressure P, temperature T and molecular weight M of the species as follows [65]:

$$J_{SiH4}[\frac{molecule}{cm^2 - \sec}] = \frac{3.51 \times 10^{22} P_{SiH4}[Torr]}{\sqrt{M_{SiH4} T}} \tag{5.12}$$

$$J_{GeH4}[\frac{molecule}{cm^2 - \sec}] = \frac{3.51 \times 10^{22} P_{GeH4}[Torr]}{\sqrt{M_{GeH4} T}} \tag{5.13}$$

where M_{SiH4} and M_{GeH4} represent molecular weight for SiH_4 (32.118 g/mol) and GeH_4 (76.67g/mol), respectively [64]. We derived the final growth rates equation with unit of [cm/second] by substituting equations (5.12)-(5.13) into equations (5.10)-(5.11):

$$R_{Si} = 0.0583 P_{SiH4} (M_{SiH4} T)^{-\frac{1}{2}} \frac{M_{Si}}{D_{Si}} k_{Si} (1-\theta)^2 \tag{5.14}$$

$$R_{Ge} = 0.0583 P_{GeH4} (M_{GeH4} T)^{-\frac{1}{2}} \frac{M_{Ge}}{D_{Ge}} k_{Ge} (1-\theta)^2 \tag{5.15}$$

Two unknown parameters in the growth rate expressions are the surface reaction rate constants k_{Si}, k_{Ge} and the fraction of the free surface sites, $(1-\theta)$. These parameters were calculated using the models reported the literature. We first discussed the calculation of the fraction of free surface sites $(1-\theta)$ proposed by Robbins et al [66]. The fraction of free surface sites $(1-\theta)$ relate to hydrogen desorption rate β from surface density N_s and sticking coefficient for hydrogen σ. The expression for free surface sites is as a following [66]:

$$1-\theta = -\frac{1}{2}\left(\frac{2N_s\beta}{\nu_m\eta\sigma} \pm \sqrt{\frac{2N_s\beta}{\nu_m\eta\sigma}\left(\frac{2N_s\beta}{\nu_m\eta\sigma}+4\right)}\right) \tag{5.16}$$

where η represents molecular density of H_2 (2.449×10^{19} molecule/cm^3). ν_m represents mean molecular velocity of H_2 at 300 K (1.78×10^5 cm/s [67]). σ represents sticking coefficient for hydrogen (1.5×10^{-9} at 600K [68]). Parameter $(\frac{\sigma}{N_s\beta})$ is a surface-dependent factor and surface density N_s can be calculated using $N_s = 2/a^2$ where a is a lattice constant. Due to a lack of data in the literature, temperature independence of ν_m and σ was assumed within the range of our deposition temperature.

A model for hydrogen desorption in SiH_4/GeH_4 system was developed by Robbins et al [66]. The hydrogen desorption rate β on Si_xGe_{1-x} films include concentration-dependent terms and exponentially related to temperature [66, 69] as a following:

$$\beta(x) = \nu\left\{x\exp\left[\frac{-E_{SiH}}{kT}\right] + (1-x)\exp\left[\frac{-E_{GeH}}{kT}\right]\right\} \tag{5.17}$$

where ν is the frequency factor = 8×10^{11} s^{-1} [70]. E_{SiH} and E_{GeH} are activation energies of H-desorption from Si and Ge sites, E_{SiH} = 197 kJ mole^{-1} and E_{GeH} = 145 kJ mole^{-1} [66, 70]. Since E_{SiH} is larger than E_{GeH}, Si-H bonds are difficult to break compared to Ge-H bonds. As Si content in SiGe alloy films increases, the fraction of surface sites covered by hydrogen increases.

5.3.4 Composition Model

Si composition x in Si_xGe_{1-x} film is dependent on SiH_4 composition in gas phase x_p and surface reaction rate constants for SiH_4 and GeH_4, k_{Si} and k_{Ge}. The expression is derived by dividing (5.8) by (5.9) [63, 69, 71]:

$$\frac{1}{x} = 1 - \frac{k_{Ge}}{k_{Si}} + \frac{k_{Ge}}{k_{Si}} \cdot \frac{1}{x_p} \tag{5.18}$$

where x_p represents SiH_4 gaseous fraction, which relates to partial pressures P_{SiH4} and P_{GeH4} as follows:

$$x_p = \frac{P_{SiH4}}{P_{SiH4} + P_{GeH4}} \tag{5.19}$$

Equation (5.18) suggests that the film composition depends on gaseous composition and adsorption process mechanisms. However, the film composition does not depend on the number of free surface sites. The adsorption reaction rate constant k_{Ge} or k_{Si} is weakly dependent on deposition temperature T [60, 63, 69]. The ratio k_{Ge}/k_{Si} relates to energy barrier of gas adsorption process as following [61-63, 71]:

$$\frac{k_{Ge}}{k_{Si}} \sim \exp(\frac{\Delta E_A}{kT}) \tag{5.20}$$

where $\Delta E_A = E_{Si} - E_{Ge}$. E_{Si} and E_{Ge} are activation energies for reactions (5.4) and (5.5). The ratio k_{Ge}/k_{Si} is a constant at 360°C. We derived the ratio and the energy difference ΔE_A using Equation (5.20). The results are shown in section 5.3.5.

5.3.5 Results and Discussion

Film composition

The relation between film composition and silane fraction (Equation 5.18) is plotted in Figure 5.4 with our experimental data from 360°C deposition and the experimental growth data at higher temperatures (550°C) reported by Meyerson et al [72]. Figure 5.4 shows that the relation between the composition and SiH_4 fractions from Equation 5.18 fitted the experimental data from both temperature. The good fit suggests that our model can be generalized to various temperatures and growth conditions.

We derived the values for the ratio k_{Ge}/k_{Si} : ~ 5.958 for 360°C and ~ 2.162 for 550°C. The value of the ratio decreased with increasing deposition temperature. This inverse relation implies that high temperature is favorable to silicon incorporation into the films. At high temperature, we expected that more Si was incorporated into the films for the same SiH_4 flow. This observation is in agreement with empirical data in SiGe deposition [71]. We used Equation (5.20) to derive

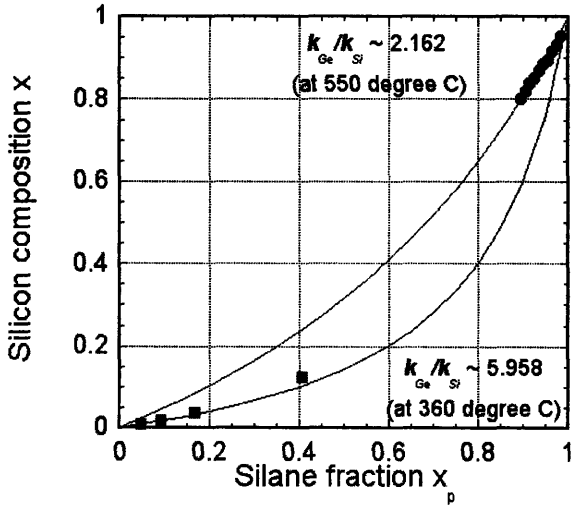

Figure 5.4 Alloy Si fraction in SiGe films x vs. gaseous SiH_4 fraction x_p. The lines represent calculation results from the model using Equation (5.18). The fitting of model to the growth date results in the ratio k_{Ge}/k_{Si} ~ 5.958 at 360°C and ~ 2.162 at 550 °C [72].

$\Delta E_A = E_{Si} - E_{Ge}$ ~ 0.14 eV. Several values for E_{Si} have been reported in the literature: 2.34 eV[73], 2.04eV[60], 1.74eV[62] and ~1.60eV[74]. The difference between E_{Si} (1.60eV[74]) and E_{Ge} (1.46 eV[61]) reported in the literature for the UHV-CVD system yielded the value of ΔE_A similar to that of ΔE_A from our finding. The agreement suggests validation of the model in Equation 5.18 that is applicable to the entire range of SiGe alloy composition.

Growth rate

The specific dependence of SiGe growth rate on SiH_4 flow, or Si composition, is shown in Figure 5.3. Calculation based on Equations (5.16)-(5.17) suggests that the dependence of growth rate on SiH_4 flow is due to hydrogen-terminated bonds on the film surface. When Si sites were terminated by hydrogen atoms, hydrogen did not easily desorb from Si sites compared to Ge sites. With increasing Si content in the films, the number of sites with H-termination also increased and available free surface sites became less. Calculated results of the surface sites in a steady state that was covered by hydrogen, θ and the desorption rate from Si sites β_{Si} and from Ge sites β_{Ge} are shown in Table 5.3.

Table 5.3 Calculated hydrogen desorption rate for Si and Ge sites, surface fraction covered by hydrogen and reaction rate constants for SiH_4.

Silicon composition x in Si_xGe_{1-x}	0.008	0.019	0.036	0.123
Total growth rate R_{SiGe} (A/hour)	552	434	329	264
Surface fraction covered by hydrogen θ	0.662	0.663	0.665	0.677
Total hydrogen desorption rate β	0.905	0.895	0.879	0.800
Hydrogen desorption rate on Si sites β_{Si}	3.66×10^{-7}	8.70×10^{-7}	1.65×10^{-6}	5.63×10^{-6}
Hydrogen desorption rate on Ge sites β_{Ge}	0.905	0.895	0.879	0.800

For all film compositions, β_{Ge} was about six orders of magnitude larger than β_{Si}, determining total H-desorption rate on the alloy film surface β. When more Si was incorporated into the films, β_{Si} was weighted more on the calculation for total desorption rate β. As a result, value of β decreased with increasing Si composition. The reduction in β yielded higher fraction of surface sites covered by hydrogen θ and caused the decrease in growth rate with increasing Si composition.

Another possibility that led to the dependence of growth rate on the composition was the exchange of hydrogen between Si site and Ge site via surface diffusion. The exchange reaction is expressed as a following [75-76]:

$$\underline{SiH}\,(s) + \underline{Ge}(s) \leftrightarrow \underline{GeH}(s) + \underline{Si}(s) \tag{5.21}$$

Since Ge-H bond is weaker compared to Si-H bond, hydrogen easily desorbs from Ge sites rather than Si sites. The exchange of hydrogen atom enhances hydrogen desorption [75-76]. Ge sites help promote the desorption reaction and enhance the growth rate. Russell et al proposed the expression for the desorption rate β, which includes the effect of the hydrogen exchange reaction [75]. Their model requires the rate constant for the exchange reaction (Equation 5.21), Ge surface fraction and Si surface fraction covered by hydrogen θ. These parameters are unknown to the experimental and literature data.

Derived sticking coefficients for SiH_4

We derived sticking coefficient S^R for SiH_4 using the equation for growth rate (Equation 5.14). By definition, sticking coefficient S^R is determined as the SiH_4 adsorption divided by SiH_4 exposure or film growth rate divided by the flux. Thus, S^R relates to k_{Si} and $(1-\theta)$ as a following:

$$S^R = k_{Si}(1-\theta)^2 \tag{5.22}$$

Figure 5.5 shows the dependence of Si growth rate R_{Si} on SiH_4 partial pressure P_{SiH4}. The linear fit to the plot results the slope of 1.146×10^{-8}. We derived S^R of 2.324×10^{-6} and compared the derived sticking coefficient S^R for SiH_4 adsorption reaction rate constant to the literature. Gates et

al reported empirical S^R of SiH_4 on Si(100)-2×1 and Si(111)-7×7 ~ 3×10^{-5} at 400°C for low SiH_4 exposure flow of < 1×10^{18} cm^{-2} or θ < 0.18 [77]. They observed reducing S^R with higher SiH_4 exposure or with more surface sites terminated by hydrogen. S^R reaches zero when surface is saturated by H coverage. Their study comments temperature independence of S^R on Si(111), but does not report the temperature dependence characteristic of S^R on Si(100). In order to compare to our derived S^R, we assumed that S^R of SiH_4 on Si(100) at 360°C was similar to that at 400°C (S^R ~ 3×10^{-5}). Our derived S^R is ~ 2.324×10^{-6}, an order of magnitude smaller than the reported S^R with H-covered surface fraction of < 0.18 [77]. Our derived S^R suggests the surface fraction was covered by hydrogen during the deposition.

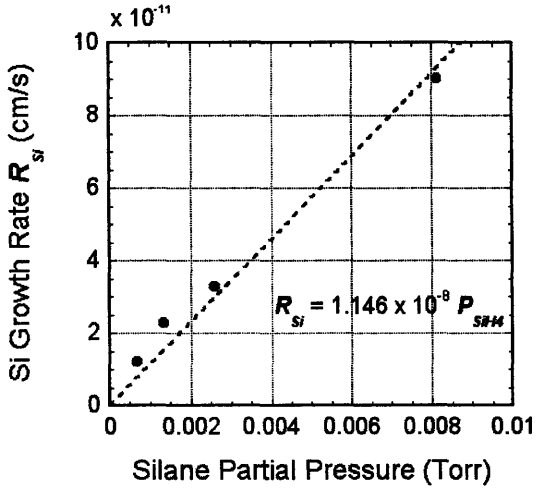

Figure 5.5 The linear dependence of Si growth rate R_{Si} on SiH_4 partial pressure P_{SiH4} in agreement with the growth rate expression (Equation 5.14). The linear fit yielded the slope of 1.146×10^{-8} or sticking coefficient S^R for SiH_4 of ~ 2.34×10^{-6} at 360°C.

5.4 High-Temperature SiGe Deposition

Remainder of SiGe films were deposited on SiGe buffer at 730°C. Growth procedure and film property of SiGe films is addressed.

5.4.1 Experimental Procedure

After SiGe buffer were deposited on Si substrates at 360°C, the furnace temperature was ramped to 730°C under H_2 ambient. Remainders of Si_xGe_{1-x} films were deposited at 730°C on $Si_{0.123}Ge_{0.877}$ buffers by varying SiH_4 flow (3 and 4.3 sccm) while keeping GeH_4 flow fixed (at 11 sccm). Processing pressure was 0.25 and 0.28 mTorr, respectively. In each deposition run, eleven wafers were loaded into the reactor. The surface roughness was checked using AFM. SiGe film composition and single-crystal quality was determined using X-Ray Diffraction (XRD) techniques on a Phillips X'Pert Pro X-Ray diffractometer, and film thickness was determined by selective etch and step profilometer. Growth conditions and resulting film property is summarized in Table 5.4.

5.4.2 Growth Rate vs. Composition

The surface roughness of Si_xGe_{1-x} films deposited on $Si_{0.123}Ge_{0.877}$ buffers was ~ 3 nm in root-mean-square. Figure 5.6 shows AFM images of the surface topography of (a) $Si_{0.11}Ge_{0.89}$ films deposited on Ge buffer and (b) $Si_{0.15}Ge_{0.85}$ films deposited on $Si_{0.123}Ge_{0.877}$ buffers.

Table 5.4 Growth parameters and resulting film property.

Sample	Lot	T (°C)	SiH_4 (sccm)	GeH_4 (sccm)	Growth rate (A/s)	Strain (%)	x_{Si} (%)
A2	2	730	4.3	11	1.039	0.240	16.35
B2	2	730	4.3	11	1.150	0.203	15.37
C1	1	730	3	11	0.990	0.263	12.01
C2	2	730	3	11	1.020	0.296	12.19
C9	9	730	3	11	0.809	0.252	13.25

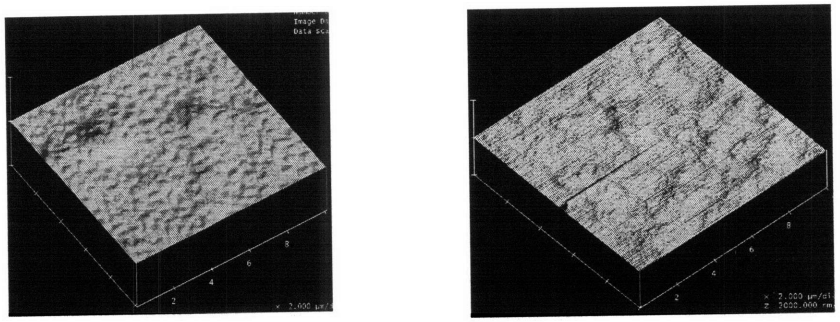

Figure 5.6 AFM images of (a) $Si_{0.11}Ge_{0.89}$ films deposited on Ge buffer and (b) $Si_{0.15}Ge_{0.85}$ films deposited on $Si_{0.123}Ge_{0.877}$ buffers.

Figure 5.6 (b) shows smooth surface of $Si_{0.15}Ge_{0.85}$ films deposited on $Si_{0.123}Ge_{0.877}$ buffers as compared to surface of $Si_{0.11}Ge_{0.89}$ films deposited on Ge buffer (Figure 5.6 a). Reduction in lattice mismatch between buffers and remainders of films decreased the surface roughness from ~ 10.6 nm (Figure 5.6 a) to ~ 3.1 nm in root-mean-square (Figure 5.6b).

Film characterization was done on multiple wafers from a single growth run. Film composition and growth rate was plotted with wafer position in the growth reactor in Figure 5.7 and Figure 5.8, respectively. Wafer position 1 represents the wafer that is closest to the gas inlet. Figure 5.7 shows that more Si is incorporated into SiGe films in wafers located further from the gas inlet. Growth rate generally increased with processing pressure, suggesting that the deposition temperature of 730°C is in diffusion-limited regime in agreement with the literature [61]. Figure 5.8 shows that the growth rate decreases when the wafer location is further from the gas inlet. Variation in thickness and composition across a single growth run batch was observed.

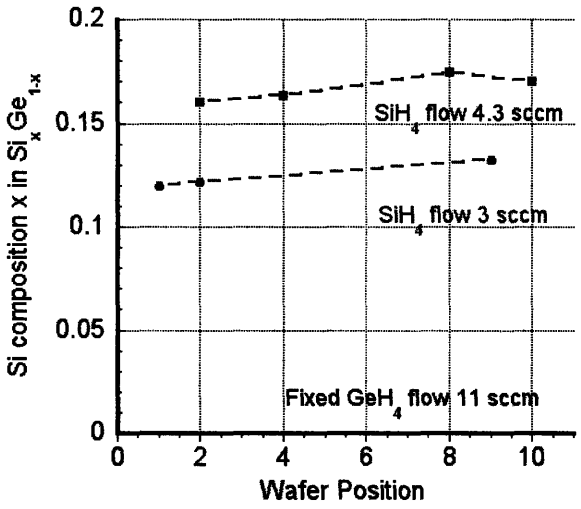

Figure 5.7 Dependence of Si composition on wafer position. Wafer position 1 was closest to the gas inlet.

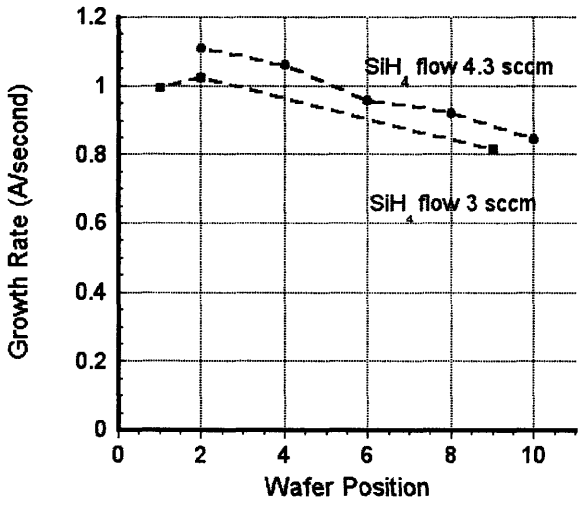

Figure 5.8 Dependence of growth rate on wafer position.

5.4.3 Strain vs. Composition

Strain and composition of the SiGe films was characterized using X-Ray Diffraction techniques. We measured SiGe (400) and SiGe (422) peak positions in θ-2θ XRD step scans of SiGe films and calculate the lattice spacing d of (400) and (422) planes. The spacing and the strain is related as a follow [24, 26]:

$$d_{400} = (1 + \varepsilon_{\perp}^{400}) \frac{a_{SiGe}}{4} \tag{5.22}$$

$$d_{422} = (1 + \varepsilon_{\perp}^{422}) \frac{a_{SiGe}}{\sqrt{24}} \tag{5.23}$$

where a represents bulk Si_xGe_{1-x} lattice constant, which is given by $5.431+0.2x+0.027x^2$ [34]. Under biaxial stress, the in-plane strain $\varepsilon_{//}$ in cubic structure is related to the out-of-plane strain $\varepsilon_{\perp}$ by [27, 78]

$$\varepsilon_{//} = -\frac{2C_{11}}{C_{12}} \varepsilon_{\perp} \tag{5.24}$$

The in-plane strain $\varepsilon_{//}$ and the out-of-plane strain $\varepsilon_{\perp}$ can be determined by the XRD data by $\varepsilon_{//} = 3\varepsilon_{\perp}^{422} - 2\varepsilon_{\perp}^{400}$ and $\varepsilon_{\perp} = \varepsilon_{\perp}^{400}$ [27]. Elastic moduli parameters C_{11} and C_{12} relate to Si composition x by $C_{11} = 128.53+37.27x$ and $C_{12} = 48.26+15.64x$ [35]. Upon cooling, tensile strain is accumulated in SiGe films due to large thermal expansion coefficient of SiGe films compared to Si substrates. Thermally induced strain in SiGe films can be calculated by taking into account the difference in thermal expansion coefficients [25,27]. We assumed that thermal expansion coefficients of SiGe are similar to that of Ge [35-36]. Theoretical value of thermally induced tensile strain was calculated ~ 0.0023 (or 0.23%).

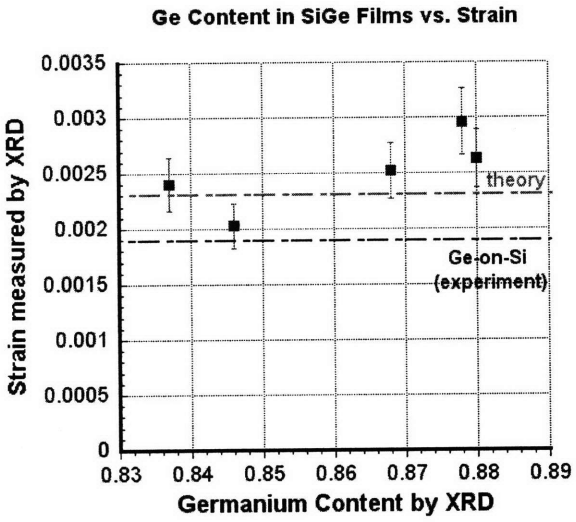

Figure 5.9 Tensile strain in SiGe films as a function of Ge content in the films.

Figure 5.9 shows the tensile strain of SiGe films as a function of germanium composition. The tensile strain in Si_xGe_{1-x} films is approximately 0.25%, which is slightly larger than the calculated strain and that of similarly grown Ge films. Relatively high strain in SiGe films suggests that the yield stress in SiGe films is larger than Ge films, in agreement with the literature report of higher yield stress in bulk crystal of SiGe compared to Ge [79-80].

5.4.4 Photoreflectance spectra

Photoreflectance (PR) measurements were performed to determine the direct gap of material [81]. Concept of photoreflectance measurements rely on the change in reflectance of materials due to the applied electric field. In the measurement, 450nm-wavelength chopped lasing light illuminated on the films to create free carriers and alter the electric field in material. Photoreflectance measurement was used to characterize the direct gap of tensile strained Ge films deposited on Si substrates [24]. The spectra show direct gap separation between light-hole and heavy-hole valence bands in tensile strained Ge films [24]. We used photoreflectance measurements to determine the direct band gap in tensile strained SiGe films. Figure 5.10 shows

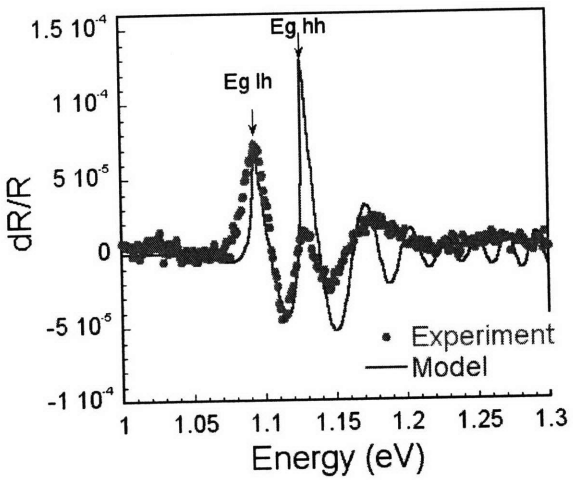

Figure 5.10 Photoreflectance spectra measured on $Si_{0.12}Ge_{0.88}$ under tensile strain of approximately 0.26%.

PR spectra measured on $Si_{0.12}Ge_{0.88}$ under tensile strain of approximately 0.26%. The PR spectra showed direct gap separation between light-hole and heavy-hole valence bands.

Doping level of Si substrates had an impact on the photoreflectance spectra measured from strained SiGe films. Figure 5.11 shows photoreflectance fringe signals from SiGe films on lightly-doped (resistivity: 5-20 Ω-cm) and heavily doped (resisitivity: 0.002-0.003 Ω-cm) substrates. Note that these films were deposited in the same deposition batch and had similar value of tensile strain measured by XRD technique. Only photoreflectance signals from SiGe films on heavily-doped substrates show five peaks, which represented separation of light-hole and heavy-hole valence band due to tensile strain whereas the signals from SiGe films deposited on lightly doped substrates did not show the separation of the valance band [25]. Weak electric field in SiGe films on lightly-doped substrates possibly attributed to missing fringes signals.

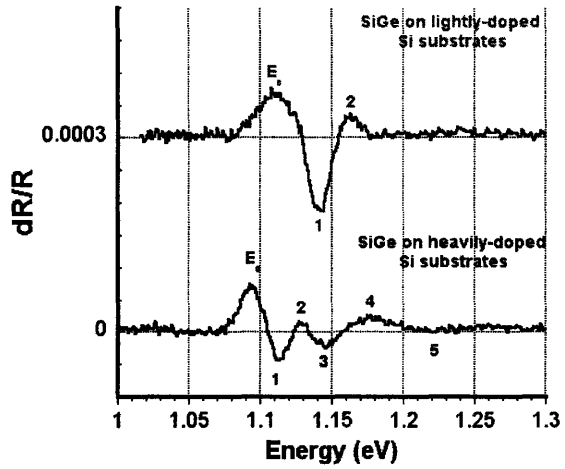

Figure 5.11 Photoreflectance fringe signals from SiGe on lightly-doped and heavily doped substrates.

5.5 Summary

Misfit strain introduces surface undulation or dislocations in epitaxial films. To reduce misfit strain between buffers and the remainders of the films, deposition of Ge-rich Si_xGe_{1-x} buffer ($0.008 \leq x \leq 0.123$) on Si (100) substrates at 360°C was developed using SiH_4 and GeH_4 source gases in UHV-CVD system. The SiGe buffers were used in the two-step growth of Si_xGe_{1-x}. Remainders of Si_xGe_{1-x} films were deposited at 730°C on the SiGe buffers. SiGe films epitaxially grown on Si substrates are tensile strained due to thermal expansion mismatch. The tensile strain in SiGe films is slightly higher than that in similarly grown Ge films and that of predicted by the theory.

Chapter 6: Device Characterization - SiGe *p-i-n* diodes and SiGe Waveguide Transmission

Electrical and optical characteristics of materials have direct impact on modulator performance. To characterize electrical and optical characteristics of SiGe, we fabricated SiGe *p-i-n* diodes and SiGe waveguides. This chapter addresses the electrical and optical characterization of SiGe films on Si substrates.

6.1 SiGe *p-i-n* diodes

6.1.1 Experimental procedure

We fabricated *p-i-n* diodes from the $Si_{0.15}Ge_{0.85}$ alloy films on Si substrates. Two annealing conditions were investigated. The first one was in-situ annealing at ~850°C for 45 minutes. The second one was the first annealing condition and followed with cyclic annealing of three cycles between 600°C and 870°C using Rapid Thermal Annealer (RTA). Process flow diagram of SiGe *p-i-n* diode is shown in Figure 6.1. Fabrication process was briefly summarized in following steps.

1) Epitaxial growth of SiGe films on p-typed boron-doped prime Si(100) wafers with resistivity of 0.002-0.003 Ω-cm followed by in-situ annealing at ~ 850°C for 45 minutes.
2) Modified RCA cleaning for SiGe films followed with deposition of 1μm thick low temperature oxide (LTO) at 400°C for SiGe passivation. The growth rate for LTO was 53 A/second. The LTO/SiGe films were annealed under N_2 ambient at 600°C for 3 hours.
3) (optional) Covered the front side of the wafers with photoresist to protect the front side while removing LTO and SiGe layer off the backside. Standard RCA cleaning for the LTO surfaces followed by annealing 3 cycles of 600°C and 870°C in RTA (30 seconds at each temperature).

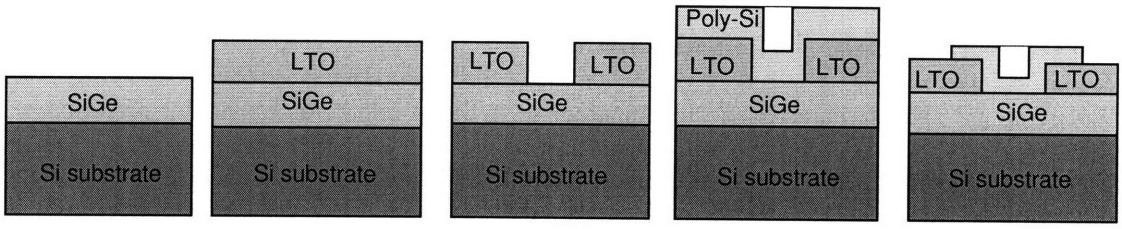

Figure 6.1 Schematic process flow of SiGe *p-i-n* diodes from SiGe deposition to selective polysilicon electrodes.

4) Opened LTO window by using reaction ion etch (RIE) and Buffer-Oxide-Etch (BOE) wet etch. Removed photoresist by plasma ashing.

5) Modified RCA cleaning for SiGe surface followed by deposition of 0.2μm thick amorphous silicon at 560°C

6) Blanket phosphorus implantation into amorphous silicon followed with activation annealing at 700°C for 3 minutes in RTA. Phosphorus implantation dose was $5\times10^{15}cm^{-2}$ at 55 keV.

7) Patterned polysilicon pads by using photolithography and reactive ion etching (RIE).

6.1.2 Results and Discussion

Electrical property of *p-i-n* diodes was characterized by I-V measurements. Figure 6.2 (a) shows the I-V measurement results of $Si_{0.15}Ge_{0.85}$ diode of 300 μm long diameter compared with Ge diode fabricated from similarly grown Ge films. The I-V characteristic from Ge diode shows rectifying behavior whereas that from $Si_{0.15}Ge_{0.85}$ diode shows high reverse-bias leakage current. I-V measurement was performed on $Si_{0.15}Ge_{0.85}$ diodes of 100, 200 and 300 μm long diameters. The results are shown in Figure 6.2 (b). Leakage current increased with diode diameters.

In order to analyze leakage current, the leakage current I^{Total} was fitted into an expression [47]:

$$I^{Total} = J^{Surface} \cdot Perimeter + J^{Bulk} \cdot Area \qquad (6.1)$$

where $J^{Surface}$ represents the surface leakage current density (per unit of diode perimeter) and J^{Bulk} represents the bulk leakage current density (per unit area). The surface leakage current density was assumed independent of bulk defect density. Values of surface leakage current density and bulk leakage current density from Ge diodes and SiGe diodes are shown in Table 6.1. Samples A

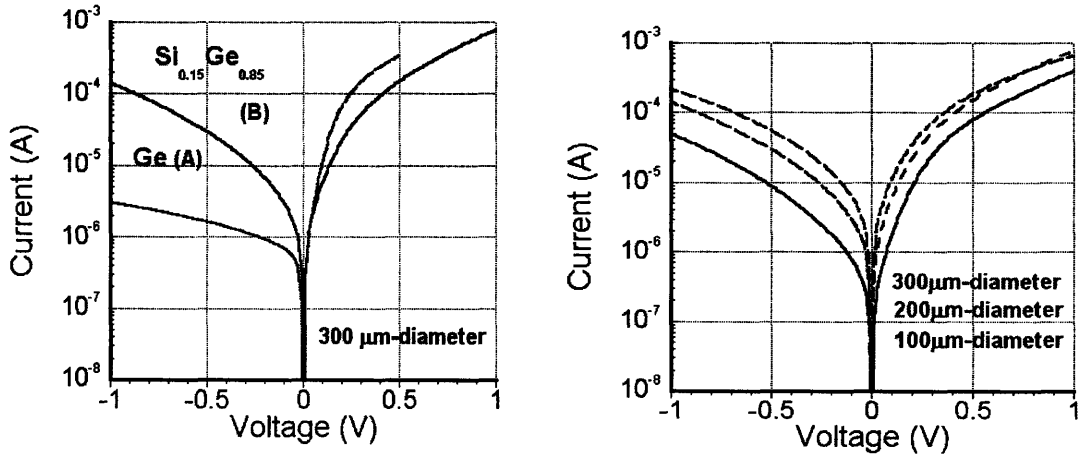

Figure 6.2 (a) compares I-V characteristics of $Si_{0.15}Ge_{0.85}$ with Ge diodes with 300 μm long diameters and (b) I-V characteristics of SiGe diodes with 100, 200, 300 μm long diameters.

Table 6.1 Surface and bulk leakage current density.

	$J_{Surface}$ (μA/cm)	J_{Bulk} (μA/cm2)
Ge diodes (4-inch Si substrates) **A**	23.9	4.93×10^{3}
SiGe diodes/ in-situ anneal	1510	2.62×10^{5}
SiGe diodes/ in-situ anneal +3cyclic RTP **B**	1660	9.01×10^{4}

and B corresponded to Ge and $Si_{0.15}Ge_{0.85}$ diodes with I-V characteristics shown in Figure 6.2 (a). Bulk leakage current of $Si_{0.15}Ge_{0.85}$ diodes is approximately an order of magnitude larger than that of Ge diodes. Bulk leakage current in Ge and SiGe diodes was analyzed in order to estimate the bulk defect density in SiGe diodes. High value of J^{Bulk} was assumed related to generation current due to bulk defect density.

Bulk defects are electrically active carrier traps, which locate in midgap and able to capture or generate free carriers. Capture or emission rates c_n in unit of $(second)^{-1}$ are given by [82]:

$$c_n = \sigma_n \upsilon_{th} n \tag{6.2}$$

where σ_n, represents a capture cross section of electron trap, υ_{th} represents average thermal velocity and n represents concentration of electrons in conduction band. The carrier emission via the bulk defects attributes to generation current density J_{gen} as given by:

$$J_{gen} = q \cdot c_n \cdot N_{Trap} = q \cdot \sigma_n \cdot v_{th} \cdot n \cdot W \cdot N_D \cdot N_{TD} \tag{6.3}$$

where W is the depletion width, N_D is threading dislocation density and N_{TD} is the number of traps per length of dislocation. The number of traps per length in dislocation was assumed 10^6 cm^{-1}, similar to that in $Si_{0.70}Ge_{0.30}$ [47]. Threading dislocations density N_D in Ge diode was checked by plane-view TEM and etch-pit-density and is reported of 2×10^7 cm^{-2} [27, 53]. Equation (6.3) was used to calculate the capture cross section σ_n in Ge-on-Si. Value of threading dislocation density and bulk leakage current density in Ge was substituted into Equation (6.3), yielding capture cross

section σ_n in Ge of 7×10^{-14} cm^2. Due to similar band structure of Ge and $Si_{0.15}Ge_{0.85}$, the capture cross section of Ge was assumed similar to the capture cross section of $Si_{0.15}Ge_{0.85}$. The calculation using Equation (6.3) and the capture cross section σ_n of Ge resulted in threading dislocation density in $Si_{0.15}Ge_{0.85}$ diode of approximately 1.7×10^9 cm^{-2}. Table 6.2 shows a summary of the parameters used in the calculation including bulk leakage current density J^{Bulk}, carrier concentrations n, threading dislocation density N_D and capture cross-section σ_n. Derived value of threading dislocation density in SiGe was ~ $1.7\times10^9 cm^{-2}$.

Threading dislocation density in $Si_{0.15}Ge_{0.85}$ films annealed in the same condition as sample B in Table 6.2 was measured using the plane-view Transmission Electron Microscopy (PV-TEM) technique. The sample was annealed in the same condition as that was used in fabrication of diode. In order to prepare for a TEM sample, the Si substrate was polished until the thickness was left approximately 50-100 μm. Then the sample was ion-milled to thin down the $Si_{0.15}Ge_{0.85}$ film for electron transmission. The JEOL 200CX TEM was used in this experiment. The sample was loaded on double-tilt axis rotation holder. The PV-TEM images were taken under double-diffraction condition where selective area diffraction pattern showed crystal orientation in the (220) direction. Figure 6.3 (a) and (b) show threading dislocations in the PV-TEM images. We counted number of threading dislocation in 30 areas of 0.5×0.5 μm^2. From the images, threading dislocations evenly distributed between 1 and 5 dislocation in each area. Number of the threading dislocation in the images yielded an average threading dislocation density of approximately $1.5\pm0.5\times10^9$ cm^{-2}. The threading dislocation density from the PV-TEM images was comparable to the threading dislocation density derived from the generation-current model. This agreement suggests a similar value of the capture cross section in Ge and $Si_{0.15}Ge_{0.85}$. The electrical property of dislocations in $Si_{0.15}Ge_{0.85}$ is similar to in Ge.

Table 6.2 Carrier concentrations, effective cross-section, density of threading dislocation and bulk leakage current in Ge and $Si_{0.15}Ge_{0.85}$ *p-i-n* diodes.

	J^{Bulk} (μA/cm2)	n (cm^{-3})	N_D (cm^{-2})	σ_n (cm^2)
Ge	4.93×10^3	2.33×10^{13}	2×10^7	$\sim 7 \times 10^{-14}$ (derived)
$Si_{0.15}Ge_{0.85}$	9.01×10^4	8×10^{12}	$\sim 1.7 \times 10^9$ (derived)	7×10^{-14}

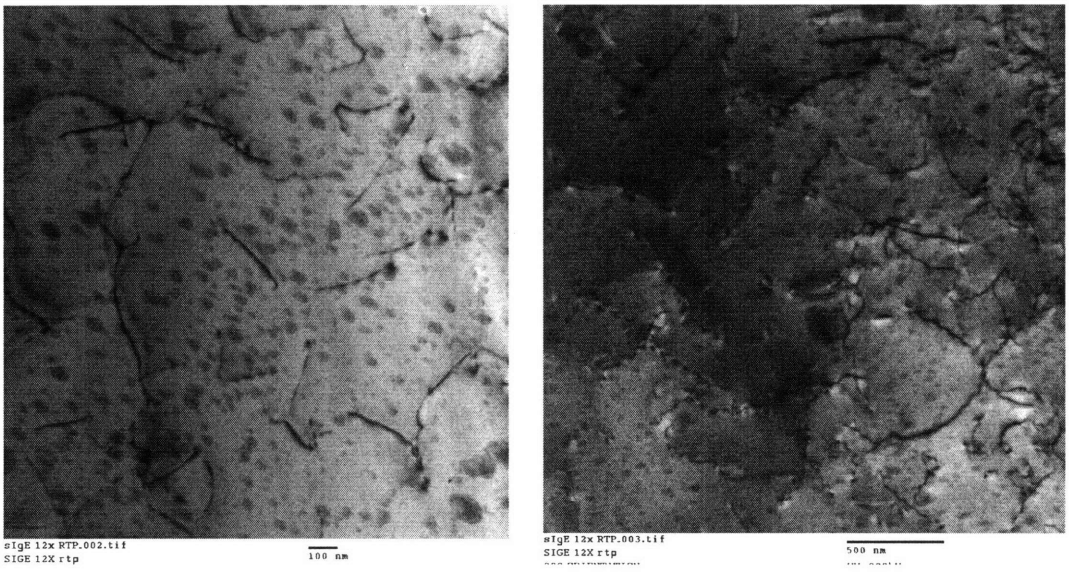

Figure 6.3 PV-TEM images showing threading dislocation density in $Si_{0.15}$ $Ge_{0.85}$ that were in-situ annealed and cyclic annealed for three cycles between 600°C and 870°C.

The PV-TEM images showed $1.5\pm0.5\times10^{9}cm^{-2}$ density of threading dislocation in annealed $Si_{0.15}Ge_{0.85}$ films. The high threading dislocation density attributed to high leakage current, which yielded ohmic-like I-V characteristic in the $Si_{0.15}Ge_{0.85}$ diodes (Figure 6.1). Bulk leakage current caused by the threading dislocation density of $1.5\pm0.5\times10^{9}cm^{-2}$ was excessively high. Model of generation current (Equation 6.3) was used to determine the limit of threading dislocation density N_D allowed for rectifying diodes. Figure 6.4 shows calculated bulk leakage current as a function of threading dislocations density. The depletion width W of 0.5 μm was assumed in the calculation. The results from the model suggest that the threading dislocation density below 5×10^{7} cm^{-2} is required to reduce the bulk leakage current of $Si_{0.15}Ge_{0.85}$ diode to the similar level to that of Ge diode.

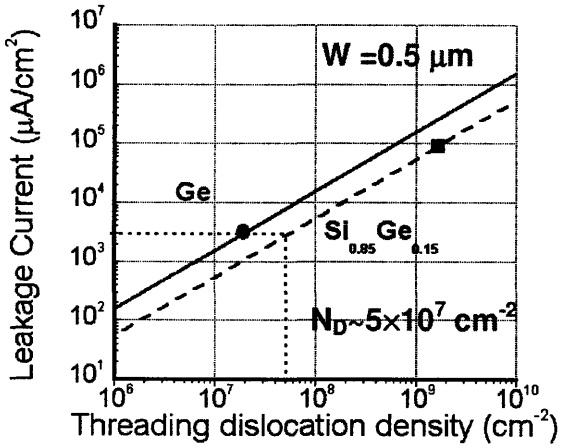

Figure 6.4 Dependence of bulk leakage current on threading dislocation density. Our model shows that the density of threading dislocation needs to be reduced below 5×10^{7} cm^{-2} for SiGe diode to reduce bulk leakage current to the same level as that of Ge diode.

6.2 SiGe Waveguides

6.2.1 SiGe rib waveguide and polysilicon/SiGe rib waveguides

We fabricated $Si_{0.15}Ge_{0.85}$ rib and polysilicon/ $Si_{0.15}Ge_{0.85}$ rib waveguides with oxide cladding. Process flow of the SiGe rib waveguides is shown in Figure 6.5. The fabrication process for the waveguides was summarized below. Optional steps were added for polysilicon/ $Si_{0.15}Ge_{0.85}$ waveguides fabrication.

1) Epitaxial growth of SiGe on p-typed boron-doped prime silicon (100) wafers with resistivity of 5-20 Ω-cm followed by in-situ annealing at ~ 850°C for 45 minutes.
2) (optional) Modified RCA cleaning for SiGe surface, deposition of 0.3μm thick amorphous silicon at 560°C.
3) Modified RCA cleaning for SiGe surface or standard RCA cleaning for amorphous Si followed with deposition of 0.2 μm thick low temperature oxide (LTO) for waveguide mask.

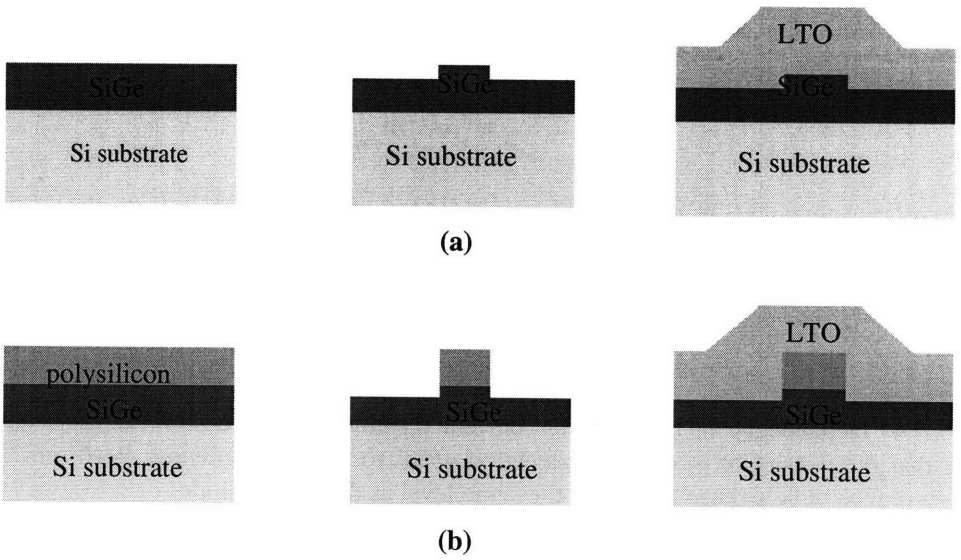

Figure 6.5 Schematic process flow of (a) SiGe rib waveguides and (b) polysilicon/SiGe rib waveguides with oxide cladding.

4) (optional) Annealed amorphous Si to crystallize into polysilicon at 600°C for 8 hours under N_2 ambient. Additional annealing at 870°C for 8 hours was performed under N_2 ambient to crystallize any residual amorphous silicon and to reduce any grain defects [83].
5) Patterned and selectively etched LTO to form hard mask by using photolithography and reaction ion etch (RIE). Photoresist was removed by plasma ashing.
6) Selectively etched polysilicon and SiGe for SiGe rib waveguides. Etch recipe for polysilicon and SiGe included HBr flow of 40 sccm and Cl_2 flow of 40 sccm under 100 mTorr pressure and 400 W power.
7) Deposition of 0.5 μm thick low temperature oxide (LTO) for waveguide cladding.

Optical throughput of the $Si_{0.15}Ge_{0.85}$ rib waveguides and the $Si_{0.15}Ge_{0.85}$/polysilicon rib waveguides with oxide cladding was measured using the Newport-JDS system with a Newport Auto-Align Station and a JDS Uniphase Swept Wavelength System (SWS). Transmission loss of waveguides was analyzed from the throughput using the cutback method, where transmission loss of waveguides was determined by comparing optical power throughput of waveguides with the varying lengths. Causes attributing to optical loss in rib waveguides are discussed in section 6.2.2.

6.2.2 Loss Mechanism

Optical loss in waveguides is attributed by one or more of the following: material absorption, light scattering due to interfaces or volumetric inhomogeneity of refractive index and coupling loss. The transmission loss L_{total} is given by a following expression [84]:

$$L_{total} = L_{\alpha}+L_{ss}+L_{vs}+L_{C} \tag{6.4}$$

where L_{α} represents material absorption. L_{ss} and L_{vs} represent light scattering due to interfaces and volumetric inhomogeneity of refractive index, respectively. L_C represents coupling loss. Since the optical absorption of $Si_{0.15}Ge_{0.85}$ at 1550 nm is less than or equal to 0.1 cm^{-1} [85], transmission loss due to material absorption L_{α} should be ~ 0.5 dB/cm. Mode calculation using

Apollo Photonics showed that transmission loss due to material absorption L_{α} and transmission loss from light scattering at interfaces L_{ss} exhibited dependence on the rib dimensions since the waveguide dimensions have an impact on values of the effective index [86]. Our experimental data and analysis showed that high density of threading dislocation also significantly attributed to the transmission loss due to inhomogeneity of refractive index L_{vs}.

6.2.3 Optical loss due to sidewall roughness

Figure 6.6 shows SEM cross-section images of the $Si_{0.15}Ge_{0.85}$ rib waveguides with (a) 0.1 μm tall rib and (b) with 0.2 μm tall rib with oxide cladding. Figure 6.6 (a)-(b) were labeled with sample A and B respectively. The optical throughput of these waveguides was measured, and the waveguide transmission was determined by the cutback method. The optical throughput of the SiGe rib waveguides with 0.2 μm tall rib (sample B) is shown in Figure 6.7. The value of the slope represented the waveguide transmission per unit length. The optical loss measured from sample A and B was 14.5 and 23 dB/cm, respectively. Increasing rib height while keeping waveguide thickness constant yielded higher intensity of optical mode localized at the sidewall imperfections, allowing for higher optical loss due to imperfections at sidewall. Table 6.3 shows a summary of waveguide dimensions of sample A and B and the corresponding transmission. Optical loss increased with the rib height, showing that the sidewall imperfection affected transmission.

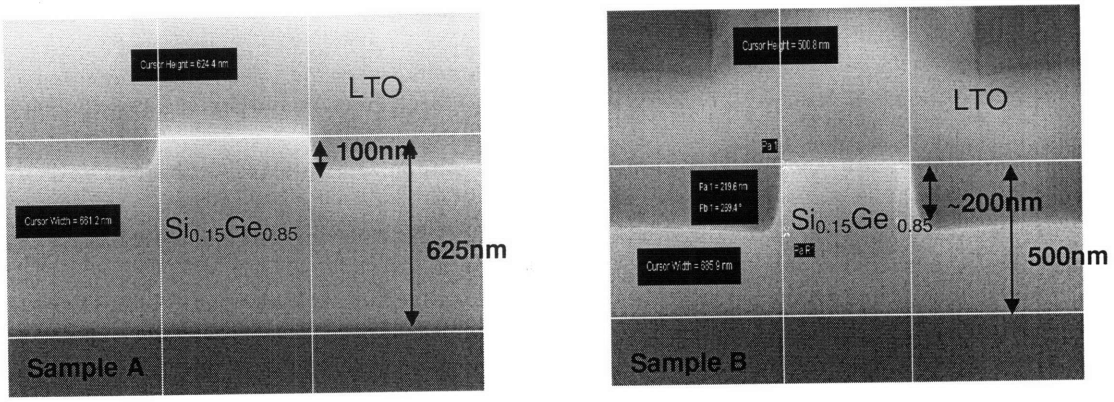

Figure 6.6 SEM cross-section images of SiGe rib waveguide with (a) 0.1μm tall rib and (b) 0.2 μm tall rib with oxide cladding.

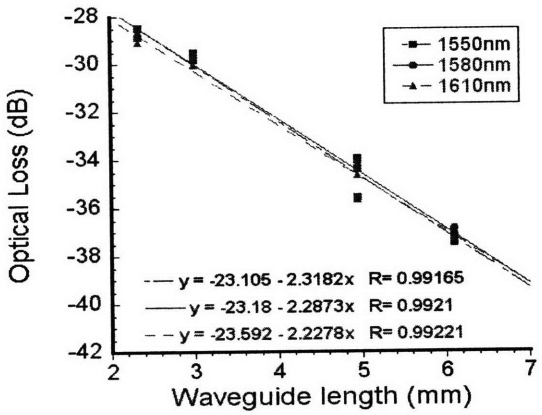

Figure 6.7 Transmission measured from SiGe rib waveguides with oxide cladding (Figure 6.6 b) as a function of waveguide length.

Table 6.3 Summary of sample dimensions and optical loss.

Samples	A	B
SiGe thickness (nm), t_{SiGe}	625	500
SiGe rib height (nm)	100	200
Optical loss (dB/cm)	14.5	23.2

6.2.4 Optical loss due to polysilicon

The $Si_{0.15}Ge_{0.85}$ rib waveguides with polysilicon deposited on the rib top showed high optical loss compared to the $Si_{0.15}Ge_{0.85}$ rib waveguides without polysilicon. Amorphous silicon was deposited at 560°C on SiGe rib structures and annealed at 600°C for 8 hours to crystallize into polysilicon. Then, some waveguides were additionally annealed at 870°C for 8 hours to reduce any grain defects. These annealing conditions were adapted for the annealing conditions in Ref. [83] with temperature constraint due to the melting temperature of $Si_{0.15}Ge_{0.85}$ (~ 960°C). Varying annealing conditions and the corresponding measured transmission of the polysilicon/ $Si_{0.15}Ge_{0.85}$ rib waveguides were summarized in Table 6.4.

Table 6.4 Summary of SiGe/polysilicon rib waveguide with oxide cladding.

Samples	C	D	E	F
SiGe thickness (nm), t_{SiGe}	630	460	560	570
Poly-Si thickness (nm), t_{poly}	260	235	248	263
Treatment for poly-Si	650°C 30 min	600°C 8 hrs	600°C 8 hrs + 870°C 8 hrs	600°C 8 hrs + 870°C 8 hrs+ DI:H_2O_2 (6:1) 1 min dip
SiGe rib height (nm)	100	150	180	220
Total rib height (nm)	360	385	428	483
Optical loss (dB/cm)	22.5	27.4	38.6	34.1

The polysilicon/$Si_{0.15}Ge_{0.85}$ waveguides with additional annealing at 870°C (sample E) showed highest optical loss of 38.6 dB/cm. The polysilicon/SiGe waveguides annealed at 870°C followed by a 1 minute dip in DI water:H_2O_2 (6:1) solution (sample F) showed lower optical loss of 34.1 dB/cm. Figure 6.8 compares SEM cross-section images of the SiGe/polysilicon waveguides (a) without H_2O_2 dip (sample E) and (b) with H_2O_2 dip (sample F). The surface of waveguides with H_2O_2 dip was smooth compared to the surface of waveguides without a treatment of H_2O_2 dip.

Measured waveguide transmission confirmed that the sidewall imperfection and the absorption from polysilicon attributed to the optical loss of $Si_{0.15}Ge_{0.85}$ rib waveguides. The lowest loss from the measurements was 14.5 dB/cm. This loss was relatively high compared to the expected loss of ~ 0.5 dB/cm, determined by the band-to-band absorption of $Si_{0.15}Ge_{0.85}$ material.

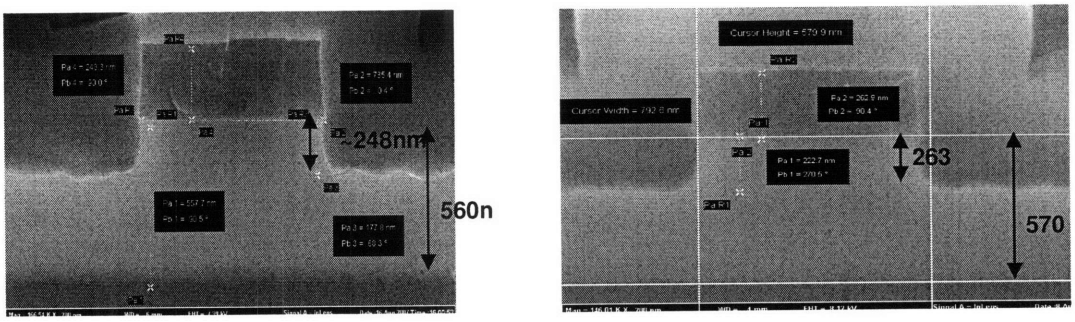

(a) **(b)**

Figure 6.8 SEM images of cross section of the $Si_{0.15}Ge_{0.85}$ /polysilicon rib waveguide (a) without wet treatment and (b) with wet treatment. Dip in hydrogen peroxide helped smoothen the $Si_{0.15}Ge_{0.85}$ surface and reduce waveguide transmission loss.

6.2.5 Optical Loss in SiGe Epitaxial Films

$Si_{0.15}Ge_{0.85}$ strip-load waveguides were fabricated without SiGe etching to ensure that only the bulk property of SiGe epitaxial films attributed to the transmission loss of the waveguides. Long strips of 1 μm thick photoresist over 0.2 μm thick LTO was fabricated on blanket SiGe films to form the relatively high-index area, along which the light wave could be guided. The LTO film was deposited and patterned in similar ways to previous SiGe waveguides. Figure 6.9 shows a schematic diagram of the strip-load SiGe waveguides with reference axes.

Mode confinement in the strip-load waveguides was analyzed by using Mode Solver Apollo Photonics and assuming light propagation in the z-direction. Figure 6.10 shows the simulation results of (a) TE mode and (b) TM mode in the strip-load waveguides where the images show waveguide cross-section in the x-y plane. The lateral width used in the simulation window was 20 μm. Due to the weak confinement in the lateral dimension, TE mode expanded wider compared to TM mode. Note that the lateral width of TE mode was larger than of TM mode. Transmission loss of these two optical modes in the SiGe strip-load waveguides was measured by the cutback method. Experimental loss of both modes was plotted in Figure 6.11. The optical loss measured at 1550, 1580 and 1610 nm of TE and TM modes was approximately 10.8-12.4 dB/cm and 8.7-9.2 dB/cm, respectively.

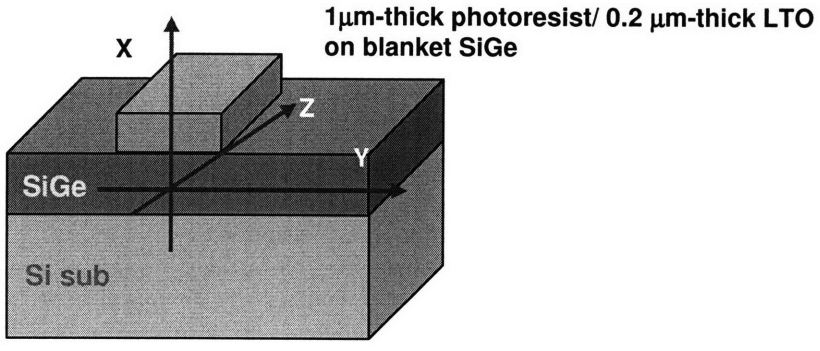

Figure 6.9 Schematic diagram of SiGe strip-load waveguide.

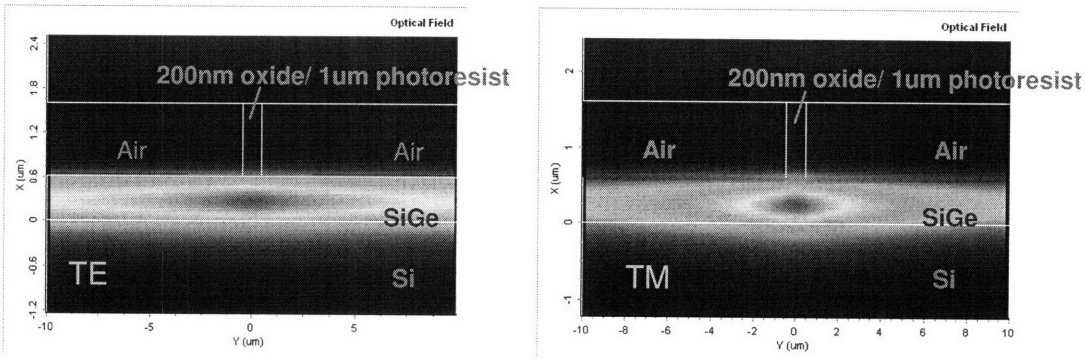

Figure 6.10 Model profiles of (a) TE mode and (b) TM mode in SiGe strip-load waveguide, simulated using a finite-difference technique. Schematic cross sectional diagram of strip-load waveguide is shown in Figure 6.09.

The value of experimental optical loss was much higher than that of calculated loss from the band-to-band transition in $Si_{0.15}Ge_{0.85}$ (~0.5 dB/cm). Since the strip-load waveguides were fabricated without etching, the measured loss should have been dominated by the bulk property of $Si_{0.15}Ge_{0.85}$. We propose that the inhomogeneity of refractive index, which was caused by threading dislocations in SiGe, attributed to the excessive optical loss. Mechanism of optical loss due to threading dislocations is discussed in section 6.2.6.

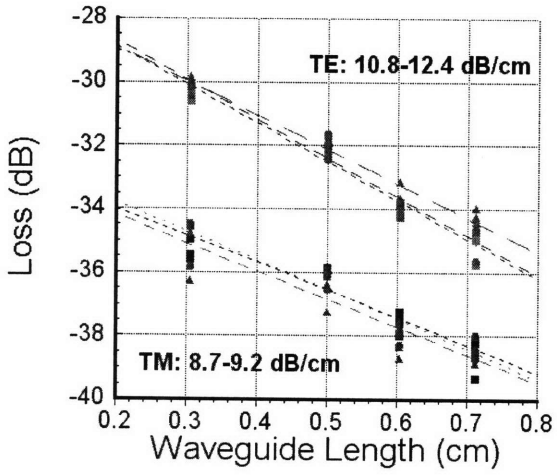

Figure 6.11 Experimental optical loss versus waveguide length. Waveguide transmission loss was extracted from the slope.

6.2.6 Light-Scattering due to dislocations

The interruption in regularity of the atomic arrangements (or dislocations) attributes to the strain fields and volume dilatation, which leads to variation in the real part of refractive index [87]. Inhomogeneity in refractive index causes some phase delay, which results a scattering loss [84]. The model of light scattering in high-dislocation-density material was based on the model proposed in Ref. [87]. Their model is used to understand the loss coefficients in bulk gallium nitride (GaN). In their model, strain field from an edge dislocation is assumed introducing the inhomogeneity of refractive index and phase delay in light propagation, causing scattering loss in dislocated materials. The dislocated materials are assumed elastically isotropic, and the dislocations are pure edge dislocations. Light propagation is assumed in the direction parallel to atomic displacement. This model was applied to estimate dislocation-introducing loss in our $Si_{0.15}Ge_{0.85}$ films.

A deviation in the assumptions from the $Si_{0.15}Ge_{0.85}$ films arose from the type of dislocations. The threading dislocation in the $Si_{0.15}Ge_{0.85}$ films are reported as "mixed" dislocation between edge and screw dislocations [45]. Figure 6.12 shows a schematic diagram of threading dislocations in SiGe films on Si substrates [43]. Threading dislocation lies at 60° to the (100) line direction and at 45° to the interface. Burgers vector of threading dislocation $b = a/2[0\bar{1}1]$ is a sum of Burgers vector of an edge dislocation $b = a/4[\bar{1}\bar{1}0]$ and of a screw dislocation $b = a/4[1\bar{1}0]$. For simplicity, threading dislocations in the model were assumed pure edge-typed dislocations.

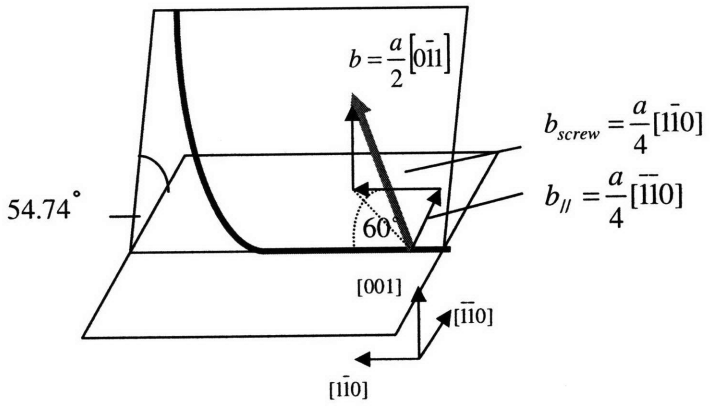

Figure 6.12 Schematic illustration of the geometry of 60° dislocation with the Burgers vector $b=\frac{a}{2}[0\bar{1}1]$ in an (001) layer [42].

Strain field from an edge dislocation attributes to volume dilation $\Delta V/V$ and causes atomic displacement in the x and y directions [87, 88]

$$u=\frac{b}{2\pi}\left(\tan^{-1}\frac{y}{x}+\frac{1}{2(1-\upsilon)}\frac{xy}{x^2+y^2}\right) \tag{6.5}$$

$$v=\frac{-b}{8\pi(1-\upsilon)}\left((1-2\upsilon)\ln(x^2+y^2)+\frac{x^2-y^2}{x^2+y^2}\right) \tag{6.6}$$

where b is the magnitude of Burgers vector and υ is the Poisson's ratio. Strain is assumed existing only in-plane (e_{zz}=0). The volume dilation is given by a sum of normal strain

$$\Delta V/V=e_{xx}+e_{yy} \tag{6.7}$$

where $e_{xx}=du/dx$ and $e_{yy}=dv/dy$. The volume dilation introduces variation in the real part of refractive index Δn by the elasto-optic effect, which is expressed in a following manner

$$\Delta n=\frac{1}{2}pn^3\Delta V/V \tag{6.8}$$

where p represents the elasto-optic coefficient (p = -0.151 for Ge). The elasto-optic coefficient for $Si_{0.15}Ge_{0.85}$ was assumed similar value as Ge. The variation in the real part of refractive index

leads to the increase in optical path length δ by integration of variations in real refractive index as a following

$$\delta = \int_{-\infty}^{\infty} \Delta n dx \tag{6.9}$$

Total difference in optical path that the light propagates is 2δ. Substituting Equations (6.5)-(6.8) into Equation (6.9), total difference in optical path length 2δ is given by

$$2\delta = -\frac{(1-2\upsilon)}{2(1-\upsilon)} n^3 pb \tag{6.10}$$

Light scattering from each dislocation is related to the difference in optical path length 2δ by a following expression

$$\frac{\Delta I}{I} = -\left(\frac{2\pi\delta}{\lambda}\right)^2 \tag{6.11}$$

Absorption coefficient is given by a sum of light scattering from all threading dislocations

$$\alpha \sim \frac{\Delta I}{I} N_D w \sim \frac{2}{3}\left(\frac{2\pi\delta}{\lambda}\right)^2 N_D w \tag{6.12}$$

where parameter $N_D w$ represents the number of dislocations in modal volume. N_D represents threading dislocation density per unit area. w represents the lateral dimension of the mode.

Dislocation-dependent optical loss was calculated as a function of the lateral dimension of the mode. Figure 6.13 shows the calculated optical loss from threading dislocation density N_D of 10^8 and 10^9 cm^{-2}. Optical loss increased with lateral dimension of the mode and threading dislocation density. Value of measured loss (8.7-9.2 dB/cm for TM mode and 10.8-12.4 dB/cm for TE mode) was labeled. The value of measured loss corresponded to threading dislocation density of 10^9 cm^{-2} and the lateral dimension of the mode was in agreement with the simulated results from Figure 6.10. The results from the model and the measurements were in agreement, showing that light scattering from dislocations attributed to optical loss in SiGe films.

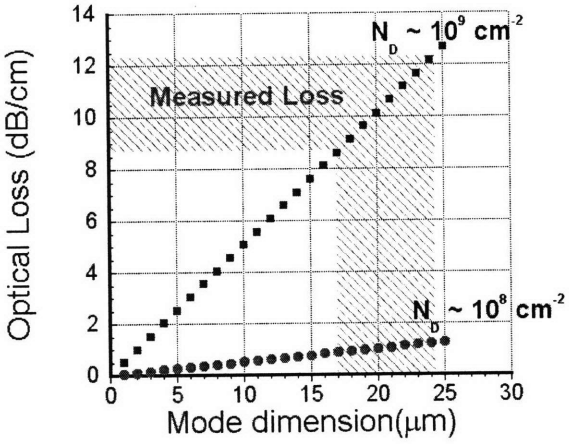

Figure 6.13 Dependence of optical loss on lateral extent of the wave.

Threading dislocation density required for optical loss below the band-to-band absorption was determined using the dislocation-dependent loss model. Figure 6.14 shows calculated transmission loss for threading dislocation density N_D ~ 10^7, 10^8 and 10^9 cm^{-2} as a function of lateral dimension of optical mode *w*. To retain transmission loss > 0.5 dB/cm, dislocation density must be less than 1×10^8 /cm^2.

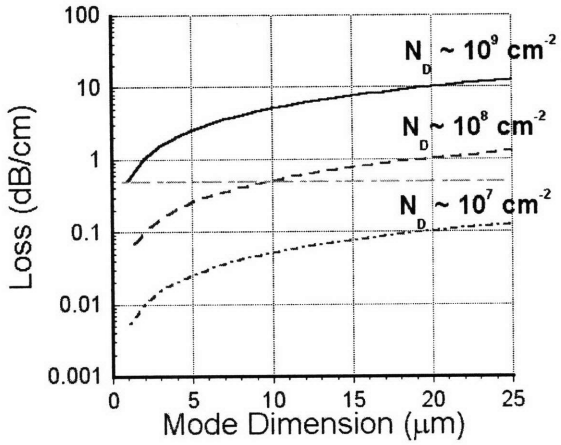

Figure 6.14 Dependence of Absorption coefficients on lateral extent of the wave and threading dislocation density.

6.3 Velocity of Dislocation Motion

Device characteristics from the $Si_{0.15}Ge_{0.85}$ *p-i-n* diodes and rib waveguides showed that high density of threading dislocation in a level of ~ 10^9 cm^{-2} deteriorated electrical and optical performance by increasing reverse-bias leakage current and introducing additional loss in the waveguides. Thermal annealing at ~ 870°C for 45 minutes reduces threading dislocation density from 10^9 to 2×10^7 cm^{-2} in Ge films by increasing glide velocity of threading dislocation and raising the probability that dislocations annihilate each other in Ge films [53, 89-90]. This annealing condition did not effectively reduce threading dislocation density in the $Si_{0.15}Ge_{0.85}$ films, similarly grown to the Ge films. Si solutes/dislocations interaction affected dislocation motion in the Ge-rich SiGe alloy. The effect of Si solutes/dislocation interaction on dislocation motion is discussed.

Dislocations in covalent semiconductors propagate by generation and motion of double kinks or kink pairs in dislocation lines [88, 91]. Glide velocity v is an exponential function of the barrier energy Q for dislocation motion and temperature T by a following manner [79, 80]

$$v = v_0\left(\frac{\tau}{\tau_0}\right)^m \exp(\frac{-Q}{kT}) \tag{6.13}$$

where τ is stress and τ_0 = 1MPa. k is the Boltzmann constant. v_0 is the pre-exponential factor that relates to the lateral velocity of kinks. m is stress exponent. Q is the barrier energy for dislocation motion and proportional to bond strength and minimum bandgap of materials [92]. The value of the barrier energy Q increases with the bandgap of materials. Addition of Si into Ge increases the bandgap, resulting in increasing barrier energy Q. The barrier energy Q of dislocation glide in Ge is 1.60 eV and in Si is 2.40eV [44].

Yonenaga et al measured dislocation velocity in bulk crystal of SiGe and derived values of m, Q and v_0 [79-80]. Figure 6.15 shows experimental dislocation velocity of SiGe bulk alloy as a function of Si content (excerpt from Ref. [79]). Dislocation velocity of Ge-rich SiGe was

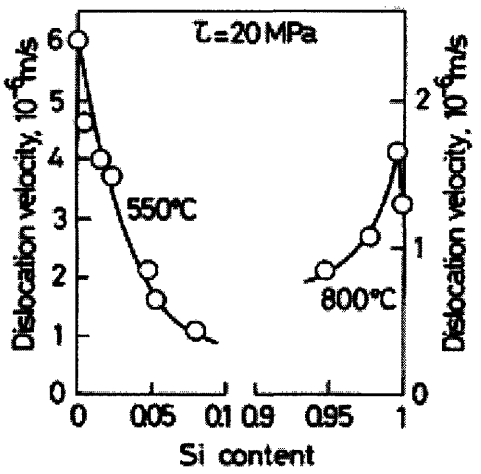

Figure 6.15 Dislocation velocity as a function of Si composition in SiGe [79].

measured at 550°C. The velocity decreases with the addition of Si into Ge-rich SiGe alloy and that of $Si_{0.08}Ge_{0.92}$ is approximately one-sixth of pure Ge. Value of the pre-exponential factors ν_0 in pure Ge and Ge-rich Si_xGe_{1-x} (x=0.047, 0.080) is reported between 230 and 460 m/s [79-80]. The value of barrier energies Q increases with addition of Si into Ge. The barrier energy Q = 1.62eV in pure Ge as compared to Q = 1.70eV in $Si_{0.08}Ge_{0.92}$ [79-80].

The stress field introduced by dislocations yielded local fluctuation of Si solute concentration in alloy matrix and affected the dislocation glide. Due to small atomic radii of Si compared to Ge, Si solutes were likely attracted to the vicinity of dislocations. The Si solute/dislocation interactions caused dislocation pinned by the solute atoms, retarding dislocation glide. Additional stress was required to release the dislocation from the solute atmosphere and allowed for the glide motion of dislocation. This model was supported by the experimental yield stress measured in SiGe bulk alloy [79-80]. Yonenaga et al show that the yield stress of $Si_{0.10}Ge_{0.90}$ and $Si_{0.40}Ge_{0.60}$ is higher than that of pure Si or Ge (Figure 6.16). High yield stress of $Si_{0.10}Ge_{0.90}$ and $Si_{0.40}Ge_{0.60}$ compared to pure Si or Ge is more pronounced at high

temperature. Yield stress of Si and Ge decreases at high temperature T as expected in elemental semiconductor, but that of the alloys is almost independent of temperature. The temperature-independent yield stress is unique characteristic for random-alloy semiconductor and may indicate the solute effect on yield stress [79, 80]. These experimental observations are in agreement with the results from kinetic Monte Carlo model by Wang et al [93]. They simulated the motion of an edge dislocation in the presence of interacting, diffusing solute atoms that have a misfit with respect to the matrix. Their results show that the dislocation motion has greatly slowed because the dislocation has captured a substantial solute cloud. They suggest the existence of a feedback mechanism that solute accumulation slows dislocation motion, and slower motion results in larger solute accumulation.

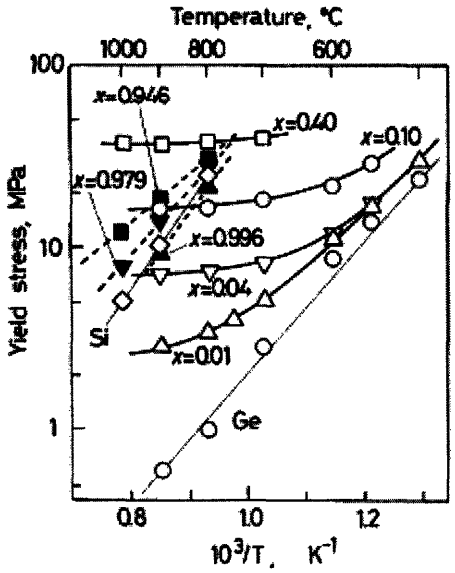

Figure 6.16 Yield stress in Si_xGe_{1-x} composition [79].

Experimental studies of dislocation velocity in binary alloys show that solute/dislocation interaction retard dislocation motion and reduce the velocity of dislocation glide [79, 80, 93]. In epitaxial films, rough surface was another factor that inhibited dislocation glide. Rough surface of SiGe film (surface roughness ~ 3.1 nm in rms) compared to Ge (surface roughness ~ 0.5 nm in rms) could block glide motion of dislocations. Fitzgerald et al show that roughened surface due to misfit strain can block dislocation motion, resulting in dislocation pile-up as shown in Figure 6.17 [49]. The dislocation pile-up imposes the strain field, inhibiting the motion of dislocations in remotely area from the pile-up.

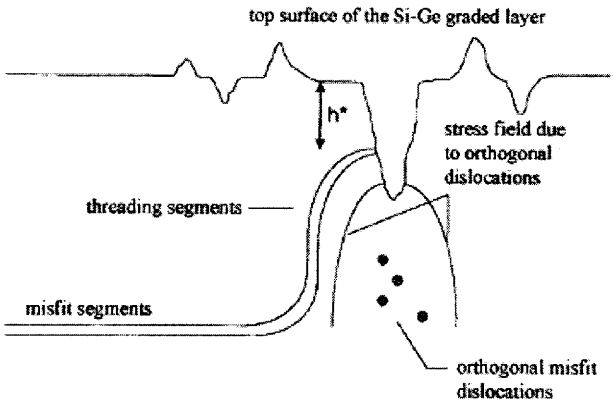

Figure 6.17 Schematic cross-sectional diagram of dislocation pile-ups by roughened surface [49].

6.4 Summary

Electrical characteristics of $Si_{0.15}Ge_{0.85}$ *p-i-n* diodes and optical characteristics of $Si_{0.15}Ge_{0.85}$ waveguides were addressed. High leakage current in $Si_{0.15}Ge_{0.85}$ *p-i-n* diodes was due to dislocation defects, consistent with measured threading dislocation density (TDD) from PV-TEM images, which showed threading dislocation density of ~ $1.5\pm0.5 \times 10^9$ cm^{-2}. Threading dislocation density below 5×10^7 cm^{-2} is required for high performance of *p-i-n* diodes. In addition, high optical loss was measured in $Si_{0.15}Ge_{0.85}$ rib waveguides and slab waveguides. The loss is due to light scattering at sidewalls and threading dislocations. Dislocation density less than 1×10^8 cm^{-2} is required for optical loss below materials' interband absorption.

Chapter 7: Summary and future work

7.1 Summary of thesis

This thesis describes the experimental confirmation of the strain-enhanced Franz-Keldysh effect in Ge layers epitaxially grown on silicon substrates, using spectral responsivity measurements. The experimental data showed strong electro-absorption effect in Ge-on-Si at 1647 nm wavelength. The Franz-Keldysh model predicts that the Ge layers on Si substrates will be the best material for phase modulation at nearly 2 μm wavelength, with a value of L_π of 3.8 mm and insertion loss of 0.4 dB.

In addition, this thesis presents the design of Si_xGe_{1-x} modulators for 1550 nm wavelength application, using the Franz-Keldysh model. The composition optimized for electroabsorption and phase modulator applications is Si_xGe_{1-x} with a value of x~0.075 and 0.135, respectively. Our calculation shows that a 50 μm long SiGe modulator yields an extinction ratio of 10 dB and a 3 dB bandwidth of > 50 GHz. Modulator length for a π-phase shift in Ge-on-Si modulator is 66 mm and the insertion loss is 5.4 dB.

To achieve high-quality Ge-rich SiGe materials for the modulator applications, deposition of Si_xGe_{1-x} ($0.008<x<0.125$) buffers at low temperature (360°C) was performed, and the growth kinetics was studied. The films were deposited on SiGe buffers to reduce lattice mismatch between the buffers and the remainders of the films, and were in-situ annealed in the same condition as was used for similarly grown Ge films for a reduction of threading dislocation density. Annealed Ge-rich SiGe films were under approximately 0.25% tensile strained, which was more strained compared to Ge-on-Si. $Si_{0.15}Ge_{0.85}$ films were used to fabricate SiGe waveguides and SiGe *p-i-n* diodes. High leakage current in $Si_{0.15}Ge_{0.85}$ *p-i-n* diodes was due to dislocation defects consistent with measured threading dislocation density (TDD) from PV-TEM images, which showed threading dislocation density of approximately $1.5\pm0.5 \times 10^9$ cm^{-2}.

Threading dislocation density below 5×10^7 cm^{-2} is required for high performance of *p-i-n* diodes. Additionally, high optical loss was measured in $Si_{0.15}Ge_{0.85}$ rib waveguides and slab waveguides. The loss is due to light scattering at sidewalls and threading dislocations. Dislocation density less than 1×10^8 cm^{-2} is required for optical loss below materials' interband absorption.

7.2 Future Work

High dislocation density of $1.5\pm0.5 \times 10^9$/cm^2 in annealed $Si_{0.15}Ge_{0.85}$ films caused high leakage current in *p-i-n* diodes and excessive optical loss in waveguides. Annealing condition that reduced the density of dislocations in Ge films did not effectively reduce the density of dislocations in the $Si_{0.15}Ge_{0.85}$ films. Si solutes/dislocations interactions retarded the glide motion of dislocations, resulting in lower probability that dislocations encountered and annihilated each other.

7.2.1 Annealing

To increase the glide velocity of dislocations, the annealing temperature T has to be increased. The expression for glide velocity in Equation (6.13) and the pre-exponential factor v_0, reported in Ref. [79-80] were used to calculate dislocation glide velocity in Ge and $Si_{0.08}Ge_{0.92}$. Calculated results showed that dislocation velocity in Ge was ~ 5 times as large that in $Si_{0.08}Ge_{0.92}$ at 850°C. Table 8.1 shows a summary of calculated dislocation velocity for Ge and $Si_{0.08}Ge_{0.92}$. We determined that temperature of ~ 950°C yielded dislocation velocity in $Si_{0.08}Ge_{0.92}$ similar to that in Ge at 850°C. Increasing glide velocity of dislocations allowed for an increase in a probability that dislocations encountered and annihilated each other.

Table 7.1 Calculated dislocation velocity for Ge and $Si_{0.08}Ge_{0.92}$

	Ge	$Si_{0.08}Ge_{0.92}$
Dislocation velocity (cm/s) at 850°C	3.9	0.86
Dislocation velocity (cm/s) at 950°C	n/a	3.6

Dislocations can be annihilated by gliding into sidewalls of patterned mesa. Luan et al demonstrates low dislocation density of ~ $2.3\pm0.2\times10^{6}$ cm^{-2} in 10μm×10μm Ge mesa compared to that of ~ $2.3\pm0.2\times10^{7}$ cm^{-2} in blanket Ge. The average threading dislocation density decreases with the decrease of mesa sidewall width. Small mesa provides short distance for dislocations to glide to dislocation sinks (mesa sidewalls) and dislocation density is reduced more effectively.

7.2.2 Constant-composition SiGe buffer deposition

Due to lattice mismatch and misfit strain, SiGe epitaxial films on Si substrates are favorable of surface undulation. During the high-temperature deposition in two-step growth processing, film surfaces tend to be undulating by atomic diffusion along the surface, or volume diffusion from the bulk of the films. To avoid surface roughening at high temperature, time allowing for the evolvement of surface undulation must be limited by increasing the growth rate or increasing the thickness of the buffer.

References

1. L.C. Kimerling, "Photonic Integration: Conquering the Last Centimeter" Plenary session presented at Integrated Photonics and Nanophotonics Research Applications (IPNRA) meeting, Salt Lake City, UT (2007).
2. R.A. Soref, "Silicon-Based Optoelectronics" *Proceedings of the IEEE,* **81** (12) p. 1687-1706 (1993).
3. L. Pavesi, "Will silicon be the photonic material of the third millennium?" *J. Phys.: Condens. Matter*, **15**, R1169-R1196 (2003).
4. B. Jalali, S. Fathpour, "Silicon Photonics" *J. Lightwave Tech.*, **24** (12) p.4600-4615 (2006).
5. A. Liu, M. Paniccia, "Advances in silicon photonic devices for silicon-based optoelectronic applications" Physica E, **35** p.223-228 (2006).
6. B. Jalali, M. Paniccia and G. Reed, "Silicon Photonics" *IEEE Microwave Magazine*, **7** (3) p.58-68 (2006).
7. K. Wakita, "Semiconductor Optical Modulators" (Kluwer Academic Publisher, Boston, 1998).
8. R. G. Hunsperger, "Integrated Optics Theory and Technology" (Springer, New York, 2002).
9. R.A. Soref and B.R. Bennett, "Electrooptical Effects in Silicon," *IEEE Journal of Quantum Electronics*, **QE-23** p.123-129 (1987).
10. A. Irace, G. Breglio, M. Iodice and A. Cutalo, "Light Modulation with Silicon Devices," in *Silicon Photonics*, L. Pavesi and D. J. Lockwood, Eds. Berlin Heidelberg: Springer-Verlag, 2004.
11. G. T. Reed and C. E. Jason Png, "Silicon optical modulators," *Materials Today*, **40**, p.40-50 (2005).
12. A. Liu, R. Jones, L. Liao, D. Samara-Rubio, D. Rubin, O. Cohen, R. Nicolaescu and M. Paniccia, "A High-speed Silicon Optical Modulator based on a metal-oxide-semiconductor capacitor" *Nature*, **427** p.615-618 (2004).
13. L. Liao, D. Samara-Rubio, M. Morse, A. Liu, D. Hodge, "High speed silicon Mach-Zehnder modulator," *Optics Express*, **13** (8) p.3129-3135 (2005).
14. T. Pinguet, V. Sadagopan, A. Mekis, B. Analui, D. Kucharski, S. Gloeckner, "A 1550 nm, 10 Gbps optical modulator with integrated driver in 130 nm CMOS," presented at 4th International Conference on Group IV Photonics, Tokyo, Japan, paper ThA2 (2007).
15. A. Liu, L. Liao, D. Rubin, H. Nguyen, B. Ciftcioglu, Y. Chetrit, N. Izhaky and M. Paniccia, "High-speed optical modulation based on carrier depletion in a silicon waveguide," *Optics Express*, **15** (2) p.660-668 (2007).
16. A. Liu, L. Liao, D. Rubin, H. Nguyen, B. Ciftcioglu, Y. Chetrit, R. Cohen, N. Izhaky, J. Basak and M. Paniccia, "Recent advances in high speed silicon optical modulator" in *Silicon Photonics II*, J.A. Kubby and G.T. Reed, Eds. Proc. of SPIE, p.64770N-1 (2007).
17. W. M. J. Green, M. J. Rooks, L. Sekaric and Y. A. Vlasov, "Ultra-compact, low RF power, 10 Gb/s silicon Mach-Zehnder modulator," *Optics Express*, **15** (25) p.17106-17113 (2007).
18. F. Gan and F.X. Kärtner, "High-Speed Silicon Electrooptic Modulator Design," *IEEE Photonics Technology Letters*, **17** (5) p.1007 (2005).
19. Q. Xu, B. Schmidt, S. Pradhan and M. Lipson, "Micrometer-scale silicon electro-optic modulator," *Nature*, **435** p.325-327 (2005).
20. Q. Xu, S. Manipatruni, B. Schmidt, J. Shakya and M. Lipson, "12.5 Gbit/s carrier-injection-based silicon micro-ring silicon modulators" *Optics Express*, **15** (2) p.430 (2007).

21. S. Wang, "Fundamentals of Semiconductor Theory and Device Physics" (Prentice Hall, 1989).
22. A. Frova and P. Handler, "Franz-Keldysh Effect in the Space-Charge Region of a Germanium p-n Junction," *Physical Review*, **137** p.1857-1861 (1965).
23. Y. Ishikawa, K. Wada, J. Liu, D. D. Cannon, H.-C. Luan, J. Michel and L. C. Kimerling, "Strain-induced band gap shrinkage in Ge grown on Si substrate," *Applied Physics Letters*, **82** p.2044-2046 (2003).
24. D. D. Cannon, J. Liu, Y. Ishikawa, K. Wada, D. T. Danielson, S. Jongthammanurak, J. Michel and L. C. Kimerling, "Tensile strained epitaxial Ge films on Si(100) substrates with potential application in *L*-band telecommunications," *Applied Physics Letters*, **84** p.906-909 (2004).
25. Y. Ishikawa, K. Wada, J. Liu, D. D. Cannon, H.-C. Luan, J. Michel and L. C. Kimerling, *Journal of Applied Physics*, **98** 013501 (2005).
26. J. Liu, D. D. Cannon, K. Wada, Y. Ishikawa, D. T. Danielson, S. Jongthammanurak, J. Michel and L. C. Kimerling, "Deformation potential constants of biaxially tensile stressed Ge epitaxial films on Si(100)," *Physical Review B*, **70** 155309 (2004).
27. J. F. Liu, D. D. Cannon, K. Wada, Y. Ishikawa, S. Jongthammanurak, D. T. Danielson, J. Michel and L. C. Kimerling, "Tensile strained Ge *p-i-n* photodetectors on Si platform for C and L band telecommunications," *Applied Physics Letters*, **87** 011110 (2005).
28. H. Shen and F. H. Pollak, "Generalized Franz-Keldysh theory of electromodulation," *Physical Review B* , **42** p.7097-7101 (1990).
29. P. Lawaetz, "Valence-band parameters in cubic semiconductors," *Physical Review B*, **4**, 3460 (1971).
30. P. K. Basu, "Theory of Optical Processing in Semiconductors: Bulk and Microstructures" (Clarendon Press, Oxford, 1997).
31. T. E. Van Eck, L. M. Walpita, W. S. C. Chang, and H. H. Wieder, *Applied Physics Letters,* **48** p.451-453 (1986).
32. S. L. Chuang, "Physics of Optoelectronics Devices" (John Wiley & Sons Inc., New York, 1995.
33. G. L. Li, P. K. L. Yu, "Optical Intensity Modulators for Digital and Analog Applications," *Journal of Lightwave Technology*, **21** (9) p.2010-2030 (2003).
34. F. Schäffler, "Silicon-Germanium (Si1-xGex)," in *Properties of Advanced Semiconductor materials*, M. E. Levinshtein, S. L. Rumyantsev and M. S. Shur, Eds. Wiley: New York, 2001.
35. *Physics of Group IV Elements and III-V Compounds*, edited by O. Madelung, Landolt-Börnstein: *Numerical Data and Functional Relationships in Science and Technology* **17a** p.449-454 (Springer: Berlin, 1982).
36. S. Jongthammanurak, J. F. Liu, K. Wada, D.D. Cannon, D.T. Danielson, D. Pan, L.C. Kimerling and J. Michel, "Large electro-optic effect in tensile strained Ge-on-Si films," *Applied Physics Letters*, **89** 161115 (2006).
37. J. F. Liu, D. Pan, S. Jongthammanurak, K. Wada, L. C. Kimerling and J. Michel, "Design of monolithically integrated GeSi electroabsorption modulators and photodetectors on an SOI platform," *Optics Express*, **15** (2) p. 623-629 (2007).
38. G. E. Betts, "LiNbO3 external modulators and their use in high performance analog links," in *RF Photonic Technology in Optical Fiber Links*, W. S. S. Change, Eds. Cambridge University Press: Cambridge, 2002.
39. D.L. Harame, S.J. Koester, G. Freeman, P. Cottrel, K. Rim, G. Dehlinger, D. Ahlgren, J.S. Dunn, D. Greenberg, A. Joseph, F. Anderson, J.-S. Rieh, S.A.S.T. Onge, D. Coolbaugh, V. Ramachandran, J.D. Cressler, and S. Subbanna, "The revolution in SiGe: impact on device electronics," *Applied Surface Science* **224** (9) (2004).

40. B.S. Meyerson, "UHV/CVD Growth of Si and Si:Ge Alloys: Chemistry, Physics, and Device Applications," *Proceedings of the IEEE*, **80** (10), p.1592 (1992).
41. F. Schäffler, "High-mobility Si and Ge structures," *Semiconductor Science and Technology*, **12** (2) p.1515 (1997).
42. E.A. Fitzgerald, "Dislocations in strained-layer epitaxy: theory, experiment, and applications," *Ann. Rev. Mater. Sci.* 25, 417 (1995).
43. R. Beanland, D.J.Dunstan, P.J. Goodhew, "Plastic relaxation and relaxed buffer layers for semiconductor epitaxy," *Advances in Physics*, 45 (2) p. 87-146 (1996).
44. M. A. Grinfeld, D. J. Srolovitz, "Stress driven morphological instabilities and islanding of epitaxial films," in *Silicon Germanium,* E. Kasper, Eds. London: INSPEC, the Institution of Electrical Engineers, 1995.
45. P. M. Mooney, "Strain Relaxation and dislocations in SiGe/Si structures," *Material Science and Engineering Reports*, **R17** p.105-146 (1996).
46. E. A. Fitzgerald, "Dislocations in strained-layer epitaxy: theory, experiment, and applications," *Materials Science Reports*, **7** p.87-142 (1991).
47. L. M. Giovane, H.-C. Luan, A. M. Agarwal, L. C. Kimerling, "Correlation between leakage current density and threading dislocation density in SiGe p-i-n diodes grown on relaxed graded buffer layers," *Applied Physics Letters*, **78** (4) p. 541-543 (2001).
48. E. A. Fitzgerald, Y.-H. Xie, M. L. Green, D. Brasen, A. R. Kortan, J. Michel, Y.-J. Mii and B. E. Weir, "Totally relaxed GexSi1-x layers with low threading dislocation densities grown on Si substrates," *Applied Physics Letters*, **59** (7) p. 811-813 (1991).
49. S. B. Samavedam and E. A. Fitzgerald, "Novel dislocation structure and surface morphology effects in relaxed Ge/Si-Ge(graded)/Si structures," *Journal of Applied Physics*, **81** (7) p.3108-3116 (1997).
50. E. A. Fitzgerald, S.B. Samavedam, Y.H. Xie and L. M. Giovane, "Influence of strain on semiconductor thin film epitaxy," *Journal of Vacuum Science Technology A*, **15** (3) p.1048-1056 (1997).
51. M.T. Currie, S.B. Samavedam, T.A. Langdo, C.W. Leitz, and E.A. Fitzgerald, *Applied Physics Letters*, **72** (14) p.1718 (1998).
52. D. M. Isaacson, C. L. Dohrman and E. A. Fitzgerald, "Deviations from ideal nucleation-limited relaxation in high-Ge content compositionally graded SiGe/Si," *Journal of Vacuum Science Technology B*, **24** (6) p.2741-2747 (2006).
53. H.-C. Luan, D. R. Lim, K.K. Lee, K.M. Chen, J.G. Sandland, K. Wada and L. Kimerling, "High-quality Ge epilayers on Si with low threading-dislocation densities," *Applied Physics Letters*, **75** p.2909-2911 (1999).
54. J.M. Hartmann, A. Abbadie, A.M. Papon, P. Holliger, G. Rolland, T. Billon, and J.M. Fedeli, M. Rouviere, L. Vivien, and S. Laval, "Reduced pressure-chemical vapor deposition of Ge thick layers on Si(001) for 1.3-1.55-μm photodetection," *Journal of Applied Physics,* **95** (10) p.5905-6003 (2004).
55. L. Colace, G. Masini, G. Assanto, H.-C. Luan, K. Wada and L. C. Kimerling, "Efficient high-speed near-infrared Ge photodetectors integrated on Si substrates," *Applied Physics Letters*, **76** (10) p.1231-1233 (2000).
56. D.D. Cannon, J. Liu, D.T. Danielson, S. Jongthammanurak, U.U. Enuha, K. Wada, J. Michel and L.C. Kimerling, "Germanium-rich silicon-germanium films epitaxially grown by ultrahigh vacuum chemical-vapor deposition directly on silicon substrates," *Applied Physics Letters*, **91** 252111 (2007).
57. D. D. Cannon *Ph.D. Thesis* (Massachusetts Institute of Technology, 2004).
58. B. J. Spencer, P. W. Voorhees and S. H. Davis, "Morphological Instability in Epitaxially Strained Dislocation-Free Solid Films," *Physical Review Letters*, **67** (26) p.3696-3699 (1991).

59. H. Gao and W. D. Nix, "Surface Roughening of Heteroepitaxial Thin Films," *Annual Review Material Science*, **29** p.173-209 (1999).
60. S.M. Gates and S.K. Kulkarni, "Kinetics of surface reactions in very low-pressure chemical vapor deposition of Si from SiH_4," *Applied Physics Letters*, **58** (25) p.2963-2965 (1991).
61. B. Cunningham, J.O. Chu and S. Akbar, "Heteroepitaxial growth of Ge on (100) Si by ultrahigh vacuum, chemical vapor deposition," *Applied Physics Letters*, **59** (27) p.3574-3576 (1991).
62. S.-M. Jang, K. Liao and R.Reif, "Chemical Vapor Deposition of Epitaxial Silicon-Germanium from Silane and Germane: I. Kinetics," *Journal of Electrochemical Society,* **142** (10) p.3513-3520 (1995).
63. D.J. Tweet, T. Tatsumi, H. Hirayama, K. Miyanaga, and K. Terashima, "Factors determining the composition of strained GeSi layer grown with disilane and germane," *Applied Physics Letters*, **65** (20) p.2579-2581 (1994).
64. D.R. Lide, ed., "CRC Handbook of Chemistry and Physics, Internet version 2007, (87th Edition)", *<http:/www.hbcpnetbase.com>*, Taylor and Francis, Boca Raton, FL, 2007.
65. D. W. Greve, "Growth of epitaxial germanium-silicon heterostructures by chemical vapour deposition," *Materials Science and Engineering B,* **18** (22) p.22-51 (1993).
66. D. J. Robbins, J. L. Glasper, A. G. Cullis, and W. Y. Leong, "A model for heterogeneous growth of $Si_{1-x}Ge_x$ films from hydrides," *Journal of Applied. Physics,*. **69** (6) p.3729-3732 (1991).
67. K. Christmann "Introduction to Surface Physical Chemistry" Springer-Verlag New York (1991).
68. M. Dürr, M. B. Raschke, E. Pehlke, and U. Höfer, *Physics Review Letters*, **86** (1), 123 (2001).
69. P. M. Garone, J. C. Sturm, P. V. Schwarz, and B. J. Wilkens, "Silicon vapour phase epitaxial growth catalysis by the presence of germane," *Applied Physics Letters,* **56** (13), p.1275-1277 (1990).
70. K. Sinniah, M. G. Sherman, L. B. Lewis, W. H. Weinberg, J. T. Yates Jr. and K. C. Janda, *Physics Review Letters,* **62** (567) (1989).
71. Y. Yasuda, Y. Koide, A. Furukawa, N. Ohshima, and S. Zaima, "Relationship between growth processes and strain relaxation in $Si_{1-x}Ge_x$ films grown on (100)Si-(2×1) surfaces by gas source molecular beam epitaxy," *Journal of Applied Physics*, **73** (5) p.2288-2293 (1993).
72. B. S. Meyerson, K. J. Uram and F. K. LeGoues, "Cooperative growth phenomena in silicon/germanium low-temperature epitaxy," *Applied Physics Letters*, **53** (25) p.2555-2557 (1988).
73. M. L. Lee, A. J. Pitera and E. A. Fitzgerald, "Growth of strained Si and strained Ge heterostructures on relaxed SiGe by ultrahigh vacuum chemical vapor deposition," *Journal of Vacuum Science and Technology B,* **22** (1) p.158-164 (2004).
74. B.S. Meyerson, "Low-temperature Si and Si:Ge epitaxy by ultrahigh-vacuum/ chemical vapor deposition: Process fundamentals," *IBM Journal Research Development,* **44** (1/2) p.132-141 (2000).
75. N.M. Russell and W.G. Breiland, "A surface kinetics model for the growth of $Si_{1-x}Ge_x$ films from SiH_4/GeH_4 mixtures," *Journal of Applied Physics*, **73** (7) p.3525-3530 (1993).
76. X. Yang and M. Tao, "A Kinetic Model for $Si_{1-x}Ge_x$ Growth from SiH_4 and GeH_4 by CVD," *Journal of Electrochemical Society*, **154** (1) p.H53-H59 (2007).
77. S. M. Gates, C. M. Greenlief, D. B. Beach and P. A. Holbert, "Decomposition of silane on Si(111)-(7×7) and Si(100)-(2×1) surfaces below 500°C," *Journal of Chemical Physics*, 95 (5) p.3144-3153 (1990).
78. M. Birkholz, "Thin Film Analysis by X-Ray scattering," (John Wiley, Chichester, 2006).

79. I. Yonenaga, "Growth and dislocation behavior in GeSi bulk alloys," *Physica B*, **273-274** p.612-615 (1999).
80. I. Yonenaga, "Dislocation Velocities and Mechanical Strength of Bulk GeSi Crystals," *Physica Staus Solidi A*, **171** (41) p.41-46 (1999).
81. F. H. Pollak, "Study of semiconductor surface and interfaces using electromodulation," *Surface and Interface Analysis*, **31** p.938-953 (2001).
82. G. L. Miller, D. V. Lang and L. C. Kimerling, "Capacitance Transient Spectroscopy," *Annual Review Materials Science*, **7** p.377-448 (1977).
83. L. Liao, D. R. Lim, A. M. Agarwal, X. Duan, K. K. Lee and L. C. Kimerling, "Optical Transmission Losses in Polycrystalline Silicon Strip Waveguides: Effects of Waveguide Dimensions, Thermal Treatment, Hydrogen Passivation and Wavelength," *Journal of Electronic Materials*, **29** (12) p.1380-1386 (2000).
84. A. G. Rickman, G. T. Reed and F. Namavar, "Silicon-on-Insulator Optical Rib Waveguide Loss and Mode Characteristics," *Journal of Lightwave Technology*, **12** (10) p.1771-1777 (1994).
85. R. Braunstein, A. R. Moore, F. Herman, "Intrinsic Optical Absorption in Germanium-Silicon Alloys," *Physical Review*, **109** (3) p.695-710 (1958).
86. R. J. Deri, E. Kapon, "Low-Loss III-V Semiconductor Optical Waveguides," *IEEE Journal of Quantum Electronics*, **27** (3) p.626-640 (1991).
87. Z. L. Liau, R. L. Aggarwal, P. A. Maki, R. J. Molnar,J. N. Walpole, R.C.Williamson and I. Melngailis, "Light scattering in high-dislocation-density GaN," *Applied Physics Letters*, **69** (12) p.1665-1668 (1996).
88. J. P.Hirth and J. Lothe, "Theory of Dislocations," (New York, John-Wiley & Sons, 1982).
89. H. C. Luan *Ph.D. Thesis* (Massachusetts Institute of Technology, 2001).
90. D. Ahn *Ph.D. Thesis* (Massachusetts Institute of Technology, 2007).
91. R. Hull, J. C. Bean, D. Bahnck, L. J. Peticolas, Jr., K. T. Short and F. C. Unterwald, "Interpretation of dislocation propagation velocities in strained Ge_xSi_{1-x}/Si (100) heterostructures by the diffusive kink pair model," *Journal of Applied Physics*, **70** (4) p.2052-2065 (1991).
92. H. Siethoff, "Correlation between the band gap of semiconductors and thermal activation parameters of plasticity," *Applied Physics Letters*, **65** (2) p.174-176 (1994).
93. Y. Wang, D. J. Srolovitz, J.M. Rickman and R. Lesar, "Dislocation motion in the presence of diffusing solutes: A Computer simulation study," Acta Materials, **48** p.2163-2175 (2000).